Volume 196, issue 7, Published 10 January 2007
ISSN 0045-7825

Computer methods in applied mechanics and engineering

Available online at
ScienceDirect
www.sciencedirect.com

http://www.elsevier.com/locate/cma

Available online at www.sciencedirect.com
ScienceDirect
ELSEVIER
Comput. Methods Appl. Mech. Engrg. 196 (2007) 1261–1277
Computer methods in applied mechanics and engineering
www.elsevier.com/locate/cma

Axisymmetric pressure boundary loading for finite deformation analysis using p-FEM

Zohar Yosibash [a,*], Stefan Hartmann [b], Ulrich Heisserer [c], Alexander Düster [c], Ernst Rank [c], Mordechai Szanto [a]

[a] *Pearlstone Center for Aeronautical Studies, Department of Mechanical Engineering, Ben-Gurion University of the Negev, Beer-Sheva, Israel*
[b] *Institute of Mechanics, University of Kassel, Germany*
[c] *Lehrstuhl für Bauinformatik, Fakultät für Bauingenieur-und Vermessungswesen, Technische Universität München, Germany*

Received 4 May 2006; received in revised form 31 August 2006; accepted 7 September 2006

Abstract

Follower loads, i.e. loads which depend on the boundary displacements by definition, frequently occur in finite deformation boundary-value problems. Restricting to axisymmetrical applications, we provide analytical and numerical solutions for a set of problems in compressible Neo-Hookean materials so to serve as benchmark problems for verifying the accuracy and efficiency of various FE methods for follower load applications. Thereafter, the weak formulation for the follower-load in 3-D domain is reduced to an axisymmetrical setting, and, subsequently, consistently linearized in the framework of p-FEMs, exploiting the blending function mapping techniques. The set of axisymmetric benchmark solutions is compared to numerical experiments, in which the results obtained by a p-FEM code are compared to these obtained by a state-of-the-art commercial h-FEM code and to the "exact" results. These demonstrate the efficiency and accuracy of p-FEMs when applied to problems in finite deformations with follower loads.

Keywords: p-FEM; Follower load; Finite strains; Hyper-elasticity; Axisymmetry

1. Introduction

Problems of continuum mechanics are usually associated with large deformations and large strains, i.e. the length, shape and orientation of the domain's boundary changes during these highly non-linear loading processes. Cold Iso-static Pressing (CIP) of metal powders is a typical example of such problems, in which the tractions on the boundary and their directions, due to the applied pressure, change according to the deformation. So far, verification examples are unavailable in general, and numerical approximations, usually by finite element methods (FEMs), are sought.

Follower-loads have been addressed for over three decades and implemented in various low-order FEMs (also known as h-FEMs), see e.g. [1–4]. However, to the best of our knowledge no analytical solutions for finite deformations are available for compressible material models, which are commonly used in FE codes, and that may serve as benchmark problems for verification of the numerical solvers. For this reason, the first step herein is to derive simple analytical and comparable solutions for axisymmetric problems which may serve as benchmark problems to assess the accuracy and efficiency of numerical approximations. In the second step, we concentrate our attention on follower loads (also known as "deformation-dependent", or "path-following" loads) in the framework of high-order FEMs (p-FEMs) [5,6], which have been shown to perform well for finite deformations analyses [7]. Following [3], the

---

[*] Corresponding author. Tel.: +972 8 6477103; fax: +972 8 6477101.
E-mail addresses: zohary@bgu.ac.il (Z. Yosibash), stefan.hartmann@uni-kassel.de (S. Hartmann), heisserer@bv.tum.de (U. Heisserer), duester@bv.tum.de (A. Düster), rank@bv.tum.de (E. Rank), mszan@ bgu.ac.il (M. Szanto).

0045-7825/$ - see front matter © 2006 Elsevier B.V. All rights reserved.
doi:10.1016/j.cma.2006.09.006

weak formulation associated with the follower-load in three-dimensional domain is reduced to an axisymmetrical setting, and, subsequently, consistently linearized in the framework of p-FEMs, exploiting the blending function mapping techniques. A set of axisymmetric numerical experiments is then addressed, in which the results obtained by a p-FEM analysis are compared to these obtained by a state-of-the-art commercial h-FEM code and to "exact" results. These demonstrate the efficiency and accuracy of p-FEMs when applied to problems in finite deformations with follower loads.

We start with notations and by deriving analytical solutions to finite deformation axisymmetric problems in Section 2. A compressible hyper-elastic material described by a Neo-Hooke type constitutive relation and loaded by pressure boundary condition (follower load) is considered. For these example problems we provide analytical solutions and numerical approximations computed by the shooting method for solving the underlying two-point boundary-value problem. In the sequel, these solutions serve as benchmark examples. Section 3 compiles the theoretical basis for the implementation of pressure loads into a FE code. In this section, we derive the weak form associated with the follower load for a three-dimensional domain, and present the consistent linearization of it. This results in two terms – a non-linear form, and a bi-nonlinear form. These two terms are restricted to axisymmetric domains. The formulation for p-axisymmetric elements is then provided in Section 4. We start this section by briefly presenting the special features of p-FE methods followed by a more detailed discussion on the implementation of the follower loads in p-FE framework. The iterative scheme for the solution of the non-linear problem is discussed. The efficiency and accuracy of our implementation is demonstrated in Section 5 on five example problems, and compared to the commercial h-FE code Abaqus.[1]

2. Verification examples in axisymmetric domains

In the following, we generate analytical/semi-analytical solutions for axisymmetric domains, based on constitutive assumptions of compressibility and isotropy. A brief description of notations for finite strain hyper-elasticity is provided followed by derivation of several analytical/semi-analytical solutions that serve as benchmarks against which the FE implementation can be verified.

The basic quantity is the deformation gradient $\boldsymbol{F} = \mathrm{Grad}\boldsymbol{\varphi}(\boldsymbol{X},t) = \frac{\partial\varphi^k(X^1,X^2,X^3,t)}{\partial X^K}\boldsymbol{g}_i \otimes \boldsymbol{G}^K$, where $\boldsymbol{x} = \boldsymbol{\varphi}(\boldsymbol{X},t)$ defines the placement of the material point $\boldsymbol{X}$ at time t. X^K, $k = 1,2,3$, are material (curvilinear) coordinates, $\boldsymbol{g}_i$ are tangent and $\boldsymbol{G}^K$ gradient vectors in current and the initial configurations. Since the most general strain-energy function for isotropic hyper-elastic material $\psi(\boldsymbol{C}) = \Psi(\mathbf{I}_{\boldsymbol{C}},\mathbf{II}_{\boldsymbol{C}},\mathbf{III}_{\boldsymbol{C}})$ or $\psi(\boldsymbol{b}) = \Psi(\mathbf{I}_{\boldsymbol{b}},\ \mathbf{II}_{\boldsymbol{b}},\mathbf{III}_{\boldsymbol{b}})$ depends on the invariants of the right Cauchy–Green tensor $\boldsymbol{C} = \boldsymbol{F}^T\boldsymbol{F}$, or the left Cauchy–Green tensor $\boldsymbol{b} = \boldsymbol{F}\boldsymbol{F}^{\mathrm{T}}$, we define

$$\mathbf{I}_{\boldsymbol{C}} = \mathrm{tr}\boldsymbol{C}, \quad \mathbf{II}_{\boldsymbol{C}} = \frac{1}{2}((\mathrm{tr}\boldsymbol{C})^2 - \mathrm{tr}\boldsymbol{C}^2),$$
$$\mathbf{III}_{\boldsymbol{C}} = \det\boldsymbol{C} = (\det\boldsymbol{F})^2 =: J^2, \tag{1}$$

$$\mathbf{I}_{\boldsymbol{b}} = \mathrm{tr}\boldsymbol{b}, \quad \mathbf{II}_{\boldsymbol{b}} = \frac{1}{2}((\mathrm{tr}\boldsymbol{b})^2 - \mathrm{tr}\boldsymbol{b}^2),$$
$$\mathbf{III}_{\boldsymbol{b}} = \det\boldsymbol{b} = (\det\boldsymbol{F})^2 =: J^2, \tag{2}$$

where $\mathrm{tr}\boldsymbol{C} = C^N_N$ (equivalently, $\mathrm{tr}\boldsymbol{b} = b^n_n$) symbolizes the trace operator. In the current configuration the Cauchy stress tensor $\boldsymbol{\sigma}$ reads

$$\boldsymbol{\sigma} = \frac{2\rho_R}{J}\frac{\mathrm{d}\psi(\boldsymbol{b})}{\mathrm{d}\boldsymbol{b}}\boldsymbol{b} = \frac{2\rho_R}{J}\boldsymbol{b}\frac{\mathrm{d}\psi(\boldsymbol{b})}{\mathrm{d}\boldsymbol{b}} = \alpha_0\boldsymbol{I} + \alpha_1\boldsymbol{b} + \alpha_2\boldsymbol{b}^2 \tag{3}$$

where ρ_R is the density in initial configuration and

$$\alpha_0 = 2\rho_R\frac{\partial\Psi}{\partial\mathbf{III}_{\boldsymbol{b}}}\mathbf{III}_{\boldsymbol{b}}^{1/2},$$
$$\alpha_1 = 2\left(\rho_R\frac{\partial\Psi}{\partial\mathbf{I}_{\boldsymbol{b}}} + \rho_R\frac{\partial\Psi}{\partial\mathbf{II}_{\boldsymbol{b}}}\mathbf{I}_{\boldsymbol{b}}\right)\mathbf{III}_{\boldsymbol{b}}^{-1/2},$$
$$\alpha_2 = -2\rho_R\frac{\partial\Psi}{\partial\mathbf{II}_{\boldsymbol{b}}}\mathbf{III}_{\boldsymbol{b}}^{-1/2}. \tag{4}$$

Here, use is made of

$$\frac{\mathrm{d}\mathbf{I}_{\boldsymbol{b}}}{\mathrm{d}\boldsymbol{b}} = \boldsymbol{I}, \quad \frac{\mathrm{d}\mathbf{II}_{\boldsymbol{b}}}{\mathrm{d}\boldsymbol{b}} = \mathbf{I}_{\boldsymbol{b}}\boldsymbol{I} - \boldsymbol{b}, \quad \frac{\mathrm{d}\mathbf{III}_{\boldsymbol{b}}}{\mathrm{d}\boldsymbol{b}} = \mathbf{III}_{\boldsymbol{b}}\boldsymbol{b}^{-1} = \mathrm{adj}\boldsymbol{b}, \tag{5}$$

which result from the application of the chain rule. The above relations are valid for any isotropic hyper-elastic material. We consider herein the simplest strain-energy function (SEF) of Neo-Hooke type:

$$\rho_R\psi(\boldsymbol{C}) = \frac{K}{2}(J-1)^2 + c_{10}(\mathbf{I}_{\overline{\boldsymbol{C}}} - 3) \tag{6}$$
$$= \frac{K}{2}(\mathbf{III}_{\boldsymbol{C}}^{1/2} - 1)^2 + c_{10}(\mathbf{I}_{\boldsymbol{C}}\mathbf{III}_{\boldsymbol{C}}^{-1/3} - 3). \tag{7}$$

$\mathbf{I}_{\overline{\boldsymbol{C}}} = \mathbf{I}_{\boldsymbol{C}}\mathbf{III}_{\boldsymbol{C}}^{-1/3}$ defines the first invariant of the unimodular right Cauchy–Green tensor $\overline{\boldsymbol{C}} = (\det\boldsymbol{C})^{-1/3}\boldsymbol{C}$ resulting from the multiplicative decomposition of the deformation gradient into a volumetric and an iso-choric part (see [8] and the literature cited therein). The specific SEF has been chosen because it describes a compressible deformation and is implemented in many standard FE codes. Previous studies addressing closed form solutions for compressible materials under finite deformations, see for example [9–11], consider special SEFs different than the common ones in standard FE codes.

The invariants of $\boldsymbol{C}$ and $\boldsymbol{b}$ are equivalent so in the following we mainly use $\boldsymbol{b}$

$$\rho_R\psi(\boldsymbol{b}) = \frac{K}{2}(J-1)^2 + c_{10}(\mathbf{I}_{\bar{\boldsymbol{b}}} - 3) \tag{8}$$
$$= \frac{K}{2}(\mathbf{III}_{\boldsymbol{b}}^{1/2} - 1)^2 + c_{10}(\mathbf{I}_{\boldsymbol{b}}\mathbf{III}_{\boldsymbol{b}}^{-1/3} - 3). \tag{9}$$

For the Neo-Hooke models (8) and (4) are explicitly expressed as:

---

[1] Abaqus is a trademark of ABAQUS, Inc., Rising Sun Mills, Providence, RI, USA.

$$\begin{aligned}\alpha_0 &= K(\mathbf{III}_{\boldsymbol{b}}^{1/2}-1)-\frac{2c_{10}}{3}\mathbf{I}_{\boldsymbol{b}}\mathbf{III}_{\boldsymbol{b}}^{-5/6},\\ \alpha_1 &= 2c_{10}\mathbf{III}_{\boldsymbol{b}}^{-5/6},\quad \alpha_2=0.\end{aligned}\tag{10}$$

2.1. Homogeneous deformation – cylinder under tension

Consider the 1×1 axisymmetric domain shown in Fig. 1, loaded at its top boundary by tension $\boldsymbol{t}=t_z\boldsymbol{e}_z=-P\boldsymbol{e}_z$ kept constant during the entire deformation, and constrained at its bottom boundary, $u_z(z=0)=0$. P defines the prescribed pressure. This is the simplest example of a follower load yielding a homogeneous deformation. The upper surface is deformation-dependent. Thus, the problem represents a follower load in which the direction of the load is preserved during the deformation but the force magnitude is not. In the case of cylindrical coordinates, the deformation reads $r=\lambda_Q R$, $\vartheta=\Theta$, and $z=\lambda Z$, where λ and λ_Q are the axial and lateral stretches, and (r,ϑ,z) and (R,Θ,Z) the cylindrical coordinates in the current and the initial configuration. The deformation gradient has the representation $\boldsymbol{F}=\lambda\boldsymbol{e}_z\otimes\boldsymbol{e}_z+\lambda_Q(\boldsymbol{e}_r\otimes\boldsymbol{e}_r+\boldsymbol{e}_\vartheta\otimes\boldsymbol{e}_\vartheta)$ with the tangent vectors $\boldsymbol{g}_1=\boldsymbol{e}_r$, $\boldsymbol{g}_2=r\boldsymbol{e}_\vartheta$, and $\boldsymbol{g}_3=\boldsymbol{e}_z$, as well as the gradient vectors $\boldsymbol{G}^1=\boldsymbol{e}_r$, $\boldsymbol{G}^2=1/R\;\boldsymbol{e}_\vartheta$, and $\boldsymbol{G}^3=\boldsymbol{e}_z$. Accordingly, the invariants (1) read

$$\mathbf{I}_{\boldsymbol{C}}=\lambda^2+2\lambda_Q^2,\quad \mathbf{II}_{\boldsymbol{C}}=(2\lambda^4+1)\lambda_Q^4,\quad \mathbf{III}_{\boldsymbol{C}}=\lambda^2\lambda_Q^4.\tag{11}$$

Because of the homogeneous deformation, the equilibrium equations are identically satisfied. The 2nd Piola–Kirchhoff stress tensor can be computed by

$$\begin{aligned}\boldsymbol{S}&=2\rho_R\frac{\mathrm{d}\psi(\boldsymbol{C})}{\mathrm{d}\boldsymbol{C}}\\ &=2\rho_{\mathrm{R}}\left(\frac{\partial\Psi}{\partial\mathbf{I}_{\boldsymbol{C}}}+\mathbf{I}_{\boldsymbol{C}}\frac{\partial\Psi}{\partial\mathbf{II}_{\boldsymbol{C}}}\right)\boldsymbol{I}-2\rho_{\mathrm{R}}\frac{\partial\Psi}{\partial\mathbf{II}_{\boldsymbol{C}}}\boldsymbol{C}+2\rho_R\mathbf{III}_{\boldsymbol{C}}\frac{\partial\Psi}{\partial\mathbf{III}_{\boldsymbol{C}}}\boldsymbol{C}^{-1},\end{aligned}$$

using the SEF (7). Having only axial stress and zero radial stress, one obtains the two equations for $S_{zz}=\sigma_{zz}\lambda_Q^2\lambda^{-1}$ and $S_{rr}=0$:

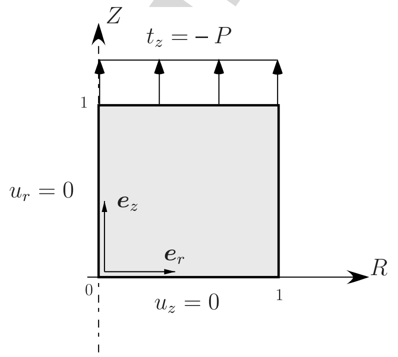

Fig. 1. Geometry and dimensions for the axisymmetric uniaxial tensile problem.

$$\begin{aligned}-P=2\rho_R\Big[&c_{10}\lambda^{-5/3}\lambda_Q^{-10/3}+\frac{K}{2}(\lambda\lambda_Q^2-\lambda^{1/3}\lambda_Q^{2/3})\\ &-\frac{1}{3}c_{10}(\lambda^2+2\lambda_Q^2)\lambda^{-1/3}\lambda_Q^{-10/3}\Big],\end{aligned}\tag{12}$$

$$\begin{aligned}0=\;&c_{10}\lambda^{-2/3}\lambda_Q^{-10/3}\left[1-\frac{1}{3}\left(\lambda^2+2\lambda_Q^2\right)\right]\\ &+\frac{K}{2}(\lambda^2\lambda_Q^2-\lambda^{4/3}\lambda_Q^{2/3}).\end{aligned}\tag{13}$$

For a given axial stretch λ, (13) represents a scalar-valued non-linear equation for the determination of the lateral stretch λ_Q. If the axial stress $\sigma_{zz}=-P$ is prescribed, (13) and (12) define two non-linear equations for the computation of λ and λ_Q. Although we solved the two linear equations numerically, see Fig. 8, we call the solution an exact solution because it can be obtained with any desired precision.

In contrast to the statement that strain-energy functions of the type (6) yield a non-physical behavior in the uniaxial tensile or compression test, see [12], this could not be observed for the Neo-Hooke model. However, if other strain-energy functions are utilized, instead of the term $U(J)=K(J-1)^2$ another volume-changing term has to be proposed in order to circumvent a non-physical behavior like a widening in lateral direction if a positive stretch is applied (see [8]).

2.2. Tube and sphere under axisymmetric boundary conditions

In order to find analytical expressions for the case of inhomogeneous deformations, it is not possible to derive a general solution of an arbitrary strain-energy function $\psi(\boldsymbol{b})$, particularly, in view of follower loads. Under the assumption of incompressibility and isotropy we can find exact solutions for finite strain hyper-elasticity represented by the thick-walled tube or sphere under internal pressure (see [13, p. 189] or [14]). In the case of compressibility two approaches are commonly utilized. The first makes use of strain-energy functions satisfying the equilibrium conditions of the underlying boundary-value problem a priori ([9–11]), which restricts the kind of strain-energy function.

The other possibility for general hyper-elasticity relations yields a one-dimensional boundary-value problem on the basis of a non-linear second order ordinary differential equation (ODE). In what follows, this approach is adopted to derive simple verification examples.

The thick-walled tube and sphere deformations under internal pressure and external tractions (see Fig. 2) are described by

$$r=f(R),\quad \vartheta=\Theta,\quad z=Z,$$

$$\Rightarrow\quad \boldsymbol{F}_t=\begin{bmatrix}f'(R)&0&0\\0&\dfrac{f(R)}{R}&0\\0&0&1\end{bmatrix}\boldsymbol{e}_k\otimes\boldsymbol{e}_l,\quad k,l=r,\vartheta,z,\tag{14}$$

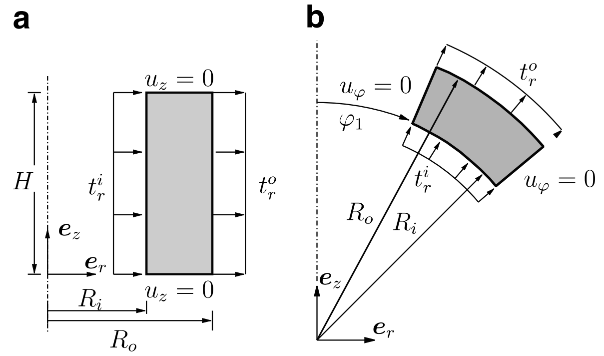

Fig. 2. Geometry and dimensions of the tube and the sphere: (a) tube and (b) sphere ($0 \leqslant \varphi < \pi, 0 \leqslant \vartheta \leqslant 2\pi$).

$$r = f(R), \quad \varphi = \Phi, \quad \vartheta = \Theta,$$
$$\Rightarrow \quad \boldsymbol{F}_s = \begin{bmatrix} f'(R) & 0 & 0 \\ 0 & \dfrac{f(R)}{R} & 0 \\ 0 & 0 & \dfrac{f(R)}{R} \end{bmatrix} \boldsymbol{e}_k \otimes \boldsymbol{e}_l, \quad k,l = r,\varphi,\vartheta. \tag{15}$$

A distinction between basis vectors $\boldsymbol{e}_k$ in the initial and the spatial configuration is not necessary in the problems investigated here.

For the sphere the tangent vectors are $\boldsymbol{g}_1 = \boldsymbol{e}_r$, $\boldsymbol{g}_2 = r\boldsymbol{e}_\varphi$, and $\boldsymbol{g}_3 = r\sin\varphi\boldsymbol{e}_\vartheta$, and the gradient vectors are $\boldsymbol{G}^1 = \boldsymbol{e}_r$, $\boldsymbol{G}^2 = (1/R)\boldsymbol{e}_\varphi$, and $\boldsymbol{G}^3 = (R\sin\Phi)^{-1}\boldsymbol{e}_\vartheta$. The deformation gradients $\boldsymbol{F}_t$ and $\boldsymbol{F}_s$ yield the left Cauchy–Green tensors

$$\boldsymbol{b}_t = \begin{bmatrix} f'^2(R) & 0 & 0 \\ 0 & \left(\dfrac{f(R)}{R}\right)^2 & 0 \\ 0 & 0 & 1 \end{bmatrix} \boldsymbol{e}_k \otimes \boldsymbol{e}_l,$$
$$\boldsymbol{b}_s = \begin{bmatrix} f'^2(R) & 0 & 0 \\ 0 & \left(\dfrac{f(R)}{R}\right)^2 & 0 \\ 0 & 0 & \left(\dfrac{f(R)}{R}\right)^2 \end{bmatrix} \boldsymbol{e}_k \otimes \boldsymbol{e}_l, \tag{16}$$

and their invariants according to (2)

$$\mathbf{I}_{\boldsymbol{b}_t} = f'^2 + \left(\frac{f}{R}\right)^2 + 1, \quad \mathbf{II}_{\boldsymbol{b}_t} = f'^2\left(\frac{f}{R}\right)^2 + f'^2 + \left(\frac{f}{R}\right)^2,$$
$$\mathbf{III}_{\boldsymbol{b}_t} = f'^2\left(\frac{f}{R}\right)^2, \tag{17}$$

and

$$\mathbf{I}_{\boldsymbol{b}_s} = f'^2 + 2\left(\frac{f}{R}\right)^2, \quad \mathbf{II}_{\boldsymbol{b}_s} = 2f'^2\left(\frac{f}{R}\right)^2 + \left(\frac{f}{R}\right)^4,$$
$$\mathbf{III}_{\boldsymbol{b}_s} = f'^2\left(\frac{f}{R}\right)^4. \tag{18}$$

The function $f(R)$, if known, determines the stress state according to (3). For the tube and the sphere the Cauchy stresses are:

$$\sigma_{rr}(R) = \alpha_0 + \alpha_1 f'^2 + \alpha_2 f'^4, \tag{19}$$
$$\sigma_{\vartheta\vartheta}(R) = \alpha_0 + \alpha_1\left(\frac{f}{R}\right)^2 + \alpha_2\left(\frac{f}{R}\right)^4 = \sigma_{\varphi\varphi}(R) \tag{20}$$
$$\sigma_{zz}(R) = \alpha_0 + \alpha_1 + \alpha_2 \tag{21}$$

although the expressions for the tube and the sphere seem to be similar, they are different due to the different invariants (17) and (18).

In addition to the kinematical relations and the constitutive equations, the stress tensor has to fulfill the equilibrium equations without body forces $\mathrm{div}\boldsymbol{\sigma} = \mathbf{0}$, expressed in the assumed curvilinear coordinates. For the stress components in (19)–(21) a single differential equation in r direction (the equations in the other two directions are satisfied identically) is obtained

$$\frac{\partial\sigma_{rr}}{\partial r} + \gamma\frac{\sigma_{rr} - \sigma_{\vartheta\vartheta}}{r} = \frac{\partial\sigma_{rr}}{\partial R}\frac{1}{f'(R)} + \gamma\frac{\sigma_{rr} - \sigma_{\vartheta\vartheta}}{f(R)} = 0,$$
$$\gamma = \begin{cases} 1, & \text{tube} \\ 2, & \text{sphere} \end{cases} \tag{22}$$

The equilibrium equation has to be supplemented by two boundary conditions (BCs) (herein we are interested in follower loads). These are the pressure at the internal surface t_r^i and tension on the outer surface t_r^o (in the initial configuration are at R_i and R_o respectively, see Fig. 2):

$$-\sigma_{rr}(R_i) = t_r^i, \quad \text{and} \quad \sigma_{rr}(R_o) = t_r^o. \tag{23}$$

The ODE for $f(R)$, is obtained by substituting (19)–(21) in (22). Considering the second term in (22):

$$\sigma_{rr}(R) - \sigma_{\vartheta\vartheta}(R) = \left(f'^2(R) - \left(\frac{f(R)}{R}\right)^2\right)$$
$$\times\left[\alpha_1 + \alpha_2\left(f'^2(R) + \left(\frac{f(R)}{R}\right)^2\right)\right]. \tag{24}$$

Remark 1. One may notice that if $f' = f/R$ then $\sigma_{rr} = \sigma_{\vartheta\vartheta}$ and the expression (24) is zero so (22) results in $\frac{\partial\sigma_{rr}}{\partial R} = 0 \Rightarrow \sigma_{rr} = \text{constant}$, i.e. a state of homogeneous deformations. Also, since (24) is zero, then also $\sigma_{\vartheta\vartheta} = \sigma_{rr} = \text{constant}$.

The first term in the equilibrium equation (22) is derived by:

$$\frac{\partial\sigma_{rr}}{\partial R} = \frac{\mathrm{d}\sigma_{rr}}{\mathrm{d}R}$$
$$= \frac{\mathrm{d}\alpha_0}{\mathrm{d}R} + \frac{\mathrm{d}\alpha_1}{\mathrm{d}R}f'^2 + \frac{\mathrm{d}\alpha_2}{\mathrm{d}R}f'^4 + 2f'f''(\alpha_1 + 2\alpha_2 f'^2). \tag{25}$$

Because $\alpha_i = \alpha_i(\mathbf{I}_{\boldsymbol{b}}, \mathbf{II}_{\boldsymbol{b}}, \mathbf{III}_{\boldsymbol{b}})$, $i = 0,1,2$, then

$$\frac{\mathrm{d}\alpha_i}{\mathrm{d}R} = \frac{\partial\alpha_i}{\partial\mathbf{I}_{\boldsymbol{b}}}\frac{\mathrm{d}\mathbf{I}_{\boldsymbol{b}}}{\mathrm{d}R} + \frac{\partial\alpha_i}{\partial\mathbf{II}_{\boldsymbol{b}}}\frac{\mathrm{d}\mathbf{II}_{\boldsymbol{b}}}{\mathrm{d}R} + \frac{\partial\alpha_i}{\partial\mathbf{III}_{\boldsymbol{b}}}\frac{\mathrm{d}\mathbf{III}_{\boldsymbol{b}}}{\mathrm{d}R} \quad \text{with}$$
$$\frac{\mathrm{d}\bullet}{\mathrm{d}R} = f'\frac{\partial\bullet}{\partial f} + f''\frac{\partial\bullet}{\partial f'} + \frac{\partial\bullet}{\partial R}, \quad \bullet = \mathbf{I}_{\boldsymbol{b}}, \mathbf{II}_{\boldsymbol{b}}, \mathbf{III}_{\boldsymbol{b}} \tag{26}$$

The 2nd order nonlinear ODE for $f(R)$ is obtained after substitution of (10) and (24)–(26) into (22) (see Appendix A):

For the tube:

$$f''f\left[10c_{10}(f^2+R^2)+f'^2\left(9K\left(\frac{ff'}{R}\right)^{2/3}f^2+4c_{10}R^2\right)\right]$$
$$=\left[2c_{10}R^2-9f^2K\left(\frac{ff'}{R}\right)^{2/3}\right]f'^4$$
$$+\frac{1}{R}\left[9f^3K\left(\frac{ff'}{R}\right)^{2/3}-20c_{10}fR^2\right]f'^3$$
$$+(20c_{10}f^2-10c_{10}R^2)f'^2-\frac{2c_{10}f}{R}(f^2-5R^2)f' \tag{27}$$

(the sequence of the terms underly no specific order). The follower load (pressure) BCs are obtained by expressing the radial Cauchy stress in terms of $f(R)$. Substituting (17) into (10) and then into (19), one obtains the required two BCs, supplementing the ODE (27):

$$\sigma_{rr}=K\left(\frac{ff'}{R}-1\right)-\frac{2c_{10}\left(f^2+(1-2f'^2)R^2\right)}{3\left(\frac{f^2f'^2}{R^2}\right)^{5/6}R^2}$$
$$\Rightarrow\begin{cases}-\sigma_{rr}(R_i)=t_r^i\\ \sigma_{rr}(R_o)=t_r^o.\end{cases} \tag{28}$$

For the sphere:

$$f''fR\left(20c_{10}f^2+4c_{10}f'^2R^2+9K\left(\frac{f^2f'}{R^2}\right)^{\frac{8}{3}}R^2\right)$$
$$=22c_{10}f'^4R^3-40c_{10}ff'^3R^2$$
$$-f'\left(-16c_{10}f^3-18fK\left(\frac{f^2f'}{R^2}\right)^{\frac{8}{3}}R^2\right)$$
$$-f'^2R\left(-2c_{10}f^2+18K\left(\frac{f^2f'}{R^2}\right)^{\frac{8}{3}}R^2\right). \tag{29}$$

Pressure boundary conditions are obtained by substituting (18) into (10) and then into (19):

$$\sigma_{rr}=K\left(-1+\frac{f^2f'}{R^2}\right)-\frac{4c_{10}\left(f^2-f'^2R^2\right)}{3\left(\frac{f^2f'}{R^2}\right)^{\frac{5}{3}}R^2}\Rightarrow\begin{cases}-\sigma_{rr}(R_i)=t_r^i\\ \sigma_{rr}(R_o)=t_r^o.\end{cases} \tag{30}$$

2.2.1. Analytical solution

The ODEs (27) and (29) are highly non-linear, and, accordingly, an analytical solution is difficult to obtain. Nevertheless, in view of Remark 1, we can obtain for a special simplified case an analytical solution. Notice that if

$$r=f(R)=AR,\quad\Rightarrow f'(R)-f(R)/R=0 \tag{31}$$

the constraint in Remark 1 is fulfilled so $\sigma_{rr}=\sigma_{\vartheta\vartheta}=$ constant, and *a homogeneous deformation is obtained with a constant stress state for any hyper-elastic material.* For $f(R)=AR$, $\rightarrow f'(R)=A$ and $f''(R)=0$ and the equilibrium equations (27) and (29) are satisfied identically. For any A the stress state is known by evaluating (19)–(21).

For the tube:

$$\sigma_{rr}=\sigma_{\vartheta\vartheta}=(A^2-1)\left(K+\frac{2c_{10}}{3A^{10/3}}\right), \tag{32}$$

$$\sigma_{zz}=(A^2-1)\left(K-\frac{4c_{10}}{3A^{10/3}}\right). \tag{33}$$

For $A>1$ we have at the inner and outer radius the same traction.

For the sphere:

$$\sigma_{rr}=\sigma_{\varphi\varphi}=\sigma_{\vartheta\vartheta}=K(A^3-1). \tag{34}$$

For the thick-walled sphere, the hydrostatic stress state is obtained.

In both solutions it becomes obvious that for given pressure a non-linear equation for computing A is necessary. However, if A is given at the inner radius (displacement control) the stress state is defined by pure function evaluations.

2.2.2. Numerical solution

For a non-homogeneous solution, the ODEs (27) or (29) in combination with the BCs (28) or (30) define two-point boundary-value problems. These are solved by the shooting method, applying of the algorithm in [15] using an explicit fifth order Runge–Kutta method with an embedded method of fourth order for step-size control. In Appendix A a general formulation for solving the tube and sphere problems for an arbitrary SEF and different BCs is described.

Herein we consider the *sphere* problem in Fig. 2(b). In this case (29) is transferred into a system of first order ODEs,

$$u_1=f(R)\qquad u_2=f'(R), \tag{35}$$

i.e.

$$u_1'(R)=u_2(R) \tag{36}$$

$$u_2'u_1R\left(20c_{10}u_1^2+4c_{10}u_2^2R^2+9K\left(\frac{u_1^2u_2}{R^2}\right)^{\frac{8}{3}}R^2\right)$$
$$=22c_{10}u_2^4R^3-40c_{10}u_1u_2^3R^2$$
$$-u_2\left[-16c_{10}u_1^3-18u_1K\left(\frac{u_1^2u_2}{R^2}\right)^{\frac{8}{3}}R^2\right]$$
$$-u_2^2\left[-2c_{10}u_1^2R+18K\left(\frac{u_1^2u_2}{R^2}\right)^{\frac{8}{3}}R^3\right]. \tag{37}$$

For traction free BCs on the outer surface R_o, and constant pressure P on R_i (as in Section 5.4) the BCs (30) read

$$P = -t_r^i = K\left(-1 + \frac{u_1^2 u_2}{R_i^2}\right) - \frac{4c_{10}\left(u_1^2 - u_2^2 R_i^2\right)}{3\left(\frac{u_1^2 u_2}{R_i^2}\right)^{\frac{5}{3}} R_i^2},$$

$$0 = K\left(-1 + \frac{u_1^2 u_2}{R_o^2}\right) - \frac{4c_{10}\left(u_1^2 - u_2^2 R_o^2\right)}{3\left(\frac{u_1^2 u_2}{R_o^2}\right)^{\frac{5}{3}} R_o^2},$$

In this case, an inhomogeneous deformation arises which serves for code verification. A solution for $P = 1$ MPa, for a sphere with $R_i = 10$ mm, $R_0 = 30$ mm, with $K = 2000$ MPa and $c_{10} = 1/2$ MPa is shown in Fig. 10.

3. Weak formulation

The aforementioned analytical and numerical solutions are aimed to serve as benchmark solutions against which FE results are to be compared to verify the accuracy and efficiency of the newly developed finite element codes. In the following, the weak formulation is developed for treating follower loads in the framework of p-FEMs, because the incorporation of blending functions, which are intrinsically embedded in p-FEM for taking into account the "exact" geometry of curvilinear boundaries, have to be considered.

Consider the domain $\Omega \subset \mathbb{R}^3$ that represents the initial configuration with $\boldsymbol{X} = (X_1, X_2, X_3)^{\mathrm{T}}$ being the position-vector to a generic point in it. A deformation $\boldsymbol{x} = \boldsymbol{\varphi}(\boldsymbol{X})$ maps the initial configuration into the current (spatial) configuration. Denote by $\mathscr{E}$ the set of admissible deformations then $\boldsymbol{\varphi} \subset \mathscr{E}$. If we assume that on a part of the boundary $\partial_P\Omega \subset \partial\Omega$ a pressure load $-P$ is activated, then according to Cauchy's theorem the traction on this boundary is

$$\boldsymbol{t} = -P\boldsymbol{n} = \boldsymbol{\sigma}\boldsymbol{n} \quad \text{on } \boldsymbol{\varphi}(\partial_P\Omega) \tag{38}$$

where $\boldsymbol{n}$ is the unit normal at the deformed body's boundary (see Fig. 3).

The departure point is the weak form for the continuum problem in the current (spatial) configuration:

$$\text{Find} \quad \boldsymbol{\varphi} \in \mathscr{E} \quad \text{such that} \quad G(\boldsymbol{\varphi}, \boldsymbol{\psi}) = 0, \quad \forall \quad \boldsymbol{\psi} \in \mathscr{E} \tag{39}$$

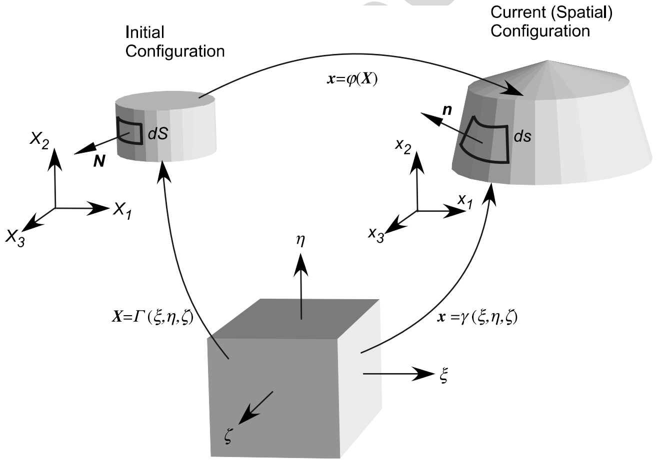

Fig. 3. Parametrization.

where

$$G(\boldsymbol{\varphi}, \boldsymbol{\psi}) = \int_{\boldsymbol{\varphi}(\Omega)} \boldsymbol{\sigma} : \nabla^S \boldsymbol{\psi}\, \mathrm{d}v - \int_{\boldsymbol{\varphi}(\Omega)} \rho \boldsymbol{b} \cdot \boldsymbol{\psi}\, \mathrm{d}v - \int_{\boldsymbol{\varphi}(\partial_P\Omega)} \boldsymbol{t} \cdot \boldsymbol{\psi}\, \mathrm{d}s \tag{40}$$

ρ is the density in the current configuration, $\boldsymbol{b}$ is the body force. $\nabla^S\boldsymbol{\psi}$ denotes the symmetric part of the current gradient (in respect to the spatial coordinates $\boldsymbol{x}$) of the admissible test functions, with components $(\nabla\boldsymbol{\psi})_{ij} = \partial\boldsymbol{\psi}_i/\partial x_j$ and $\nabla^S\boldsymbol{\psi} = 1/2(\nabla\boldsymbol{\psi} + \nabla^T\boldsymbol{\psi})$. Thus,

$$\nabla\boldsymbol{\psi} \overset{\mathrm{def}}{=} \frac{\partial\boldsymbol{\psi}_i}{\partial x_j} = \frac{\partial\boldsymbol{\psi}_i}{\partial X_k}\frac{\partial X_k}{\partial x_j} = \mathrm{Grad}\boldsymbol{\psi}\mathbf{F}^{-1}. \tag{41}$$

If both the deformation-independent traction and the deformation-dependent pressure (follower loading in general changes orientation according to the displacements) are prescribed on $\partial_P\Omega$, the term associated with tractions in (40) is split into two contributions, one due to constant tractions in space, and one because of pressure (38). Herein, we address the term $\overline{G}$ associated to the pressure normal to the boundary:

$$\overline{G}(\boldsymbol{\varphi}, \boldsymbol{\psi}) = \int_{\boldsymbol{\varphi}(\partial_P\Omega)} -P\boldsymbol{n} \cdot \boldsymbol{\psi}\, \mathrm{d}s. \tag{42}$$

3.1. Pressure loading – representation in a referential configuration

We define a referential configuration given by $\Omega_{\text{referential}} = \{\boldsymbol{\xi}^{\mathrm{T}} \overset{\mathrm{def}}{=} (\xi\eta\zeta) | -1 \leqslant \xi \leqslant 1, -1 \leqslant \eta \leqslant 1, -1 \leqslant \zeta \leqslant 1\}$, and let $\boldsymbol{\Gamma}$ denote a mapping from this referential configuration into the initial configuration $\mathbf{X} = \boldsymbol{\Gamma}(\boldsymbol{\xi})$. Assume that the face $\xi, \eta, \zeta = 1$ of the referential configuration is mapped onto the face of $\partial_P\Omega$ where the pressure is applied, then the unit normal vector $\boldsymbol{N}$ is given by

$$\boldsymbol{N} = \frac{\frac{\partial\boldsymbol{\Gamma}}{\partial\xi} \times \frac{\partial\boldsymbol{\Gamma}}{\partial\eta}}{\left\|\frac{\partial\boldsymbol{\Gamma}}{\partial\xi} \times \frac{\partial\boldsymbol{\Gamma}}{\partial\eta}\right\|_{L^2}} \tag{43}$$

and an infinitesimal surface element $\mathrm{d}S$ on $\partial_P\Omega$ is

$$\mathrm{d}S = \left\|\frac{\partial\boldsymbol{\Gamma}}{\partial\xi} \times \frac{\partial\boldsymbol{\Gamma}}{\partial\eta}\right\|_{L^2} \mathrm{d}\xi\,\mathrm{d}\eta. \tag{44}$$

Thus, the unit normal times $\mathrm{d}S$ is obtained in terms of the referential coordinates as

$$(\boldsymbol{N}\mathrm{d}S) = \left(\frac{\partial\boldsymbol{\Gamma}}{\partial\xi} \times \frac{\partial\boldsymbol{\Gamma}}{\partial\eta}\right)_{\zeta=1} \mathrm{d}\xi\,\mathrm{d}\eta. \tag{45}$$

The spatial description of the same boundary with respect to the referential variables is obtained by setting $\boldsymbol{\gamma} = \boldsymbol{\varphi}(\boldsymbol{\Gamma}(\xi, \eta, \zeta = 1))$. Using the chain rule one obtains

$$\frac{\partial\boldsymbol{\gamma}}{\partial\xi} = \frac{\partial\boldsymbol{\varphi}}{\partial X_i}\frac{\partial X_i}{\partial\xi} = \boldsymbol{F}\frac{\partial\boldsymbol{\Gamma}}{\partial\xi}, \quad \frac{\partial\boldsymbol{\gamma}}{\partial\eta} = \frac{\partial\boldsymbol{\varphi}}{\partial X_i}\frac{\partial X_i}{\partial\eta} = \boldsymbol{F}\frac{\partial\boldsymbol{\Gamma}}{\partial\eta}, \tag{46}$$

consequently, the unit normal vector times an infinitesimal surface area corresponding to the initial configuration is

$$(\boldsymbol{n}\,\mathrm{d}s) = \left(\frac{\partial\gamma}{\partial\xi}\times\frac{\partial\gamma}{\partial\eta}\right)_{\zeta=1}\mathrm{d}\,\xi\mathrm{d}\eta = \left(\boldsymbol{F}\frac{\partial\boldsymbol{\Gamma}}{\partial\xi}\times\boldsymbol{F}\frac{\partial\boldsymbol{\Gamma}}{\partial\eta}\right)_{\zeta=1}\mathrm{d}\,\xi\mathrm{d}\eta. \tag{47}$$

An alternative representation, see the implementation issues in Section 4, expresses the deformed configuration by $\gamma(\boldsymbol{\xi}) = \boldsymbol{\Gamma}(\boldsymbol{\xi}) + \boldsymbol{\varphi}(\boldsymbol{X})$. Hence we arrive at

$$(\boldsymbol{n}\,\mathrm{d}s) = \left(\frac{\partial\gamma}{\partial\xi}\times\frac{\partial\gamma}{\partial\eta}\right)_{\zeta=1}\mathrm{d}\xi\,\mathrm{d}\eta = \left[\left(\frac{\partial\boldsymbol{\Gamma}}{\partial\xi}+\frac{\partial\boldsymbol{\varphi}}{\partial\xi}\right)\times\left(\frac{\partial\boldsymbol{\Gamma}}{\partial\eta}+\frac{\partial\boldsymbol{\varphi}}{\partial\eta}\right)\right]_{\zeta=1}\mathrm{d}\xi\,\mathrm{d}\eta. \tag{48}$$

Substituting (47) in (42) one obtains:

$$\overline{G}(\boldsymbol{\varphi},\boldsymbol{\psi}) = -\int_{-1}^{1}\int_{-1}^{1} P\left[\left(\frac{\partial\gamma}{\partial\xi}\times\frac{\partial\gamma}{\partial\eta}\right)\cdot\boldsymbol{\psi}\right]_{\zeta=1}\mathrm{d}\xi\,\mathrm{d}\eta. \tag{49}$$

3.2. Linearization of the weak form

The expression (49) is non-linear because the integrand involves the unknown deformation $\boldsymbol{\varphi}$ as can be clearly seen in Eq. (48). Non-linear problems of this type may be solved by an iterative Newton–Raphson process. There, for a given solution estimate $\boldsymbol{\varphi}^{(i)}$ (and its corresponding mapping $\gamma^{(i)}$) at iteration i, a correction $\boldsymbol{\mu}^{(i)} \overset{\mathrm{def}}{=} \boldsymbol{\varphi}^{(i+1)} - \boldsymbol{\varphi}^{(i)}$ is obtained by a linear approximation

$$\overline{G}(\boldsymbol{\varphi}^{(i+1)},\boldsymbol{\psi}) \approx \overline{G}(\boldsymbol{\varphi}^{(i)},\boldsymbol{\psi}) + D\overline{G}(\boldsymbol{\varphi}^{(i)},\boldsymbol{\psi})[\boldsymbol{\mu}^{(i)}] \tag{50}$$

where $D\overline{G}(\boldsymbol{\varphi}^{(i)},\boldsymbol{\psi})[\boldsymbol{\mu}^{(i)}]$ is the directional derivative of $\overline{G}$ in the direction of $\boldsymbol{\mu}^{(i)}$. In the consistent linearization procedure of (49) two terms are generated, the first is a regular linear form, and the second is a tangential form derived in this subsection. As the Newton–Raphson iterative scheme is known to converge only in a certain range close to the solution it may be necessary to apply the load in k steps or use more sophisticated approaches to improve the convergence. In the former case we apply instead of the entire pressure P, a fraction of it $j\alpha P$, with $\alpha = 1/k \leqslant 1$. The equation $G(\boldsymbol{\varphi},\boldsymbol{\psi},j\alpha) = 0$ is solved for a prescribed load level $j\alpha P$. After convergence the next load increment is applied $(j+1)\alpha P$ until the desired total load is reached $k\alpha P$.

Define a map $\boldsymbol{\mu}^{(i)}(\boldsymbol{x})$ acting on the $\boldsymbol{\varphi}^{(i)}(\mathbf{X})$ configuration, and let ε be an arbitrary small scalar. We construct a one parameter family of configurations that represents the transformation to the configuration, $\boldsymbol{\varphi}_{\varepsilon}^{(i)}$

$$\boldsymbol{\varphi}_{\varepsilon}^{(i)}(\mathbf{X}) = \boldsymbol{\varphi}^{(i)}(\mathbf{X}) + \varepsilon\boldsymbol{\mu}^{(i)}(\boldsymbol{x}) \tag{51}$$

and let $\gamma_{\varepsilon}^{(i)} \overset{\mathrm{def}}{=} \gamma^{(i)} + \varepsilon\boldsymbol{\mu}^{(i)}$ be the parametrization of the surface $\boldsymbol{\varphi}_{\varepsilon}^{(i)}$. Then the directional derivative (Gateaux derivative) of $\overline{G}$ is obtained by

$$D\overline{G}(\boldsymbol{\varphi}^{(i)},\boldsymbol{\psi},\alpha)[\boldsymbol{\mu}^{(i)}] = \left.\frac{\mathrm{d}}{\mathrm{d}\varepsilon}\right|_{\varepsilon=0}\overline{G}(\boldsymbol{\varphi}^{(i)}+\varepsilon\boldsymbol{\mu}^{(i)},\boldsymbol{\psi}). \tag{52}$$

Substituting $\gamma_{\varepsilon}^{(i)} = \gamma^{(i)} + \varepsilon\boldsymbol{\mu}^{(i)}$ into (49) and using the product rule, the consistent linearization of $\overline{G}$ in the direction of $\boldsymbol{\mu}$ is obtained,

$$D\overline{G}(\boldsymbol{\varphi}^{(i)},\boldsymbol{\psi},\alpha)[\boldsymbol{\mu}^{(i)}] = -\int_{-1}^{1}\int_{-1}^{1}P(\alpha)\left\{\left[\frac{\partial\boldsymbol{\mu}^{(i)}}{\partial\xi}\times\frac{\partial\gamma^{(i)}}{\partial\eta}+\frac{\partial\gamma^{(i)}}{\partial\xi}\times\frac{\partial\boldsymbol{\mu}^{(i)}}{\partial\eta}\right]\cdot\boldsymbol{\psi}\right\}_{\zeta=1}\mathrm{d}\xi\,\mathrm{d}\eta. \tag{53}$$

Remark 2. From the finite element implementation point of view, a follower load produces two contributions in the linearization process – the linear form (49), based on which a load vector will be computed, and the consistent tangential derivative (53) which, in general, will yield an unsymmetric tangent matrix. A detailed discussion under which circumstances the tangent matrix will be symmetric or unsymmetric can be found in [16,17].

Remark 3. Note that in the iterative solution scheme (Newton-type iterative scheme) both (49) and (53) depend on the configuration defined by $\gamma^{(i)}$. However, this is known in each iteration from the previous one and a vector function to be found is $\boldsymbol{\mu}^{(i)}$, which is the addition to $\gamma^{(i)}$ at iteration i.

3.3. Axisymmetric domains

In the axisymmetric case the three-dimensional problem is reduced to a two dimensional cross-section at an arbitrary plane, $\vartheta = 0$ for example, see Fig. 4. The referential configuration is the unit square $[-1,1]\times[-1,1]$ and its boundary is a one-dimensional curve in the initial or current configuration, mapped from the line $-1 \leqslant \xi \leqslant 1$ in the referential configuration. We use the notation:

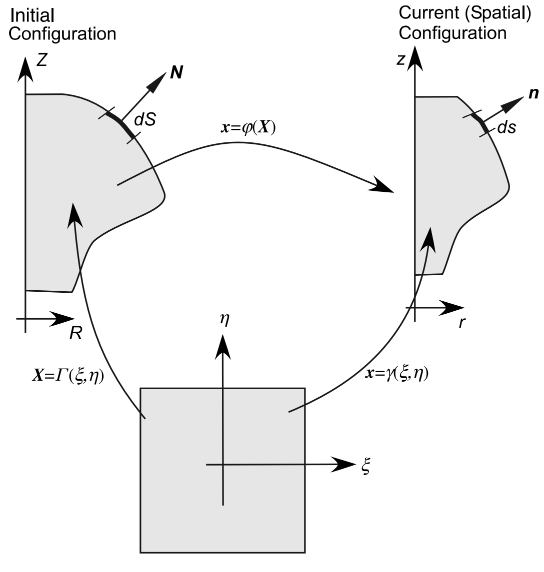

Fig. 4. Axisymmetric parametrization.

$$\boldsymbol{x}=\boldsymbol{\varphi}(R,Z),\quad \text{with}\begin{cases} r=\varphi_r(R,Z)=\gamma_r(\xi,\eta)\\ z=\varphi_z(R,Z)=\gamma_z(\xi,\eta)\end{cases}, \tag{54}$$

$\boldsymbol{g}_3=r\mathbf{e}_\vartheta=\gamma_r\boldsymbol{e}_\vartheta$, where $\boldsymbol{e}_k$, $k=r,\vartheta,z$, is a unit vector in the cylindrical coordinate system. The outward normal vector to the boundary ($\eta=1$ for example) in this case is obtained by the cross product of the tangent vector along the coordinate ϑ, $\boldsymbol{g}_3$ with the tangent vector to $\mathrm{d}S$:

$$(\mathbf{n}\,\mathrm{d}s)=\mathbf{g}_3\times\left.\frac{\partial\boldsymbol{\gamma}}{\partial\xi}\right|_{\eta=1}\mathrm{d}\xi=\begin{pmatrix}-\dfrac{\partial\gamma_z}{\partial\xi}\\ \dfrac{\partial\gamma_r}{\partial\xi}\end{pmatrix}_{\eta=1}\gamma_r(\xi,1)\,\mathrm{d}\xi. \tag{55}$$

Substituting (55) in (49), one obtains the load vector for the axisymmetric case and load level α

$$\overline{G}(\boldsymbol{\varphi},\boldsymbol{\psi},\alpha)=-2\pi\int_{-1}^{1}P(\alpha)\left[\left(-\frac{\partial\gamma_z}{\partial\xi},\frac{\partial\gamma_r}{\partial\xi}\right)^{\mathrm{T}}\cdot\boldsymbol{\psi}\gamma_r(\xi,1)\right]_{\eta=1}\mathrm{d}\xi. \tag{56}$$

Similarly to (52), the directional derivative in the axisymmetric case is

$$\begin{aligned}
&D\overline{G}(\boldsymbol{\varphi}^{(i)},\boldsymbol{\psi},\alpha)[\boldsymbol{\mu}^{(i)}]\\
&=\left.\frac{\mathrm{d}}{\mathrm{d}\varepsilon}\right|_{\varepsilon=0}\overline{G}(\boldsymbol{\varphi}^{(i)}+\varepsilon\boldsymbol{\mu}^{(i)},\boldsymbol{\psi},\alpha)=-2\pi\int_{\partial\Omega_P}P(\alpha)\left.\frac{\mathrm{d}}{\mathrm{d}\varepsilon}\right|_{\varepsilon=0}\left[\boldsymbol{n}_\varepsilon^{(i)}\mathrm{d}s_\varepsilon\right]\cdot\boldsymbol{\psi}\\
&=-2\pi\int_{-1}^{1}P(\alpha)\left.\frac{\mathrm{d}}{\mathrm{d}\varepsilon}\right|_{\varepsilon=0}\left\{\left[(\gamma_r^{(i)}+\varepsilon\mu_r^{(i)})\boldsymbol{e}_\vartheta\times\left(\frac{\partial\boldsymbol{\gamma}^{(i)}}{\partial\xi}+\varepsilon\frac{\partial\boldsymbol{\mu}^{(i)}}{\partial\xi}\right)\mathrm{d}\xi\right]\cdot\boldsymbol{\psi}\right\}_{\eta=1}\\
&=-2\pi\int_{-1}^{1}P(\alpha)\left.\frac{\mathrm{d}}{\mathrm{d}\varepsilon}\right|_{\varepsilon=0}\left\{\left[\gamma_r^{(i)}\boldsymbol{e}_\vartheta\times\frac{\partial\boldsymbol{\gamma}^{(i)}}{\partial\xi}+\varepsilon\left(\gamma_r^{(i)}\boldsymbol{e}_\vartheta\times\frac{\partial\boldsymbol{\mu}^{(i)}}{\partial\xi}+\mu_r^{(i)}\boldsymbol{e}_\vartheta\times\frac{\partial\boldsymbol{\gamma}^{(i)}}{\partial\xi}\right)\right.\right.\\
&\qquad\left.\left.+\varepsilon^2(\mu_r^{(i)}\boldsymbol{e}_\vartheta)\times\frac{\partial\boldsymbol{\mu}^{(i)}}{\partial\xi}\right]\cdot\boldsymbol{\psi}\right\}_{\eta=1}\mathrm{d}\xi\\
&=-2\pi\int_{-1}^{1}P(\alpha)\left[\left(\gamma_r^{(i)}\boldsymbol{e}_\vartheta\times\frac{\partial\boldsymbol{\mu}^{(i)}}{\partial\xi}+\mu_r^{(i)}\boldsymbol{e}_\vartheta\times\frac{\partial\boldsymbol{\gamma}^{(i)}}{\partial\xi}\right)\cdot\boldsymbol{\psi}\right]_{\eta=1}\mathrm{d}\xi.
\end{aligned} \tag{57}$$

We finally obtain the consistent linearization of $\overline{G}$ in the direction of $\boldsymbol{\mu}^{(i)}$ for the axisymmetric domain:

$$\begin{aligned}
&D\overline{G}(\boldsymbol{\varphi}^{(i)},\boldsymbol{\psi},\alpha)[\boldsymbol{\mu}^{(i)}]\\
&\quad=-2\pi\int_{-1}^{1}P(\alpha)\left[\begin{pmatrix}-\dfrac{\partial\mu_z^{(i)}}{\partial\xi}\gamma_r^{(i)}-\dfrac{\partial\gamma_z^{(i)}}{\partial\xi}\mu_r^{(i)}\\ \dfrac{\partial\mu_r^{(i)}}{\partial\xi}\gamma_r^{(i)}+\dfrac{\partial\gamma_r^{(i)}}{\partial\xi}\mu_r^{(i)}\end{pmatrix}\cdot\boldsymbol{\psi}\right]_{\eta=1}\mathrm{d}\xi.
\end{aligned} \tag{58}$$

Remark 4. Notice that the variation of the radius $\gamma_r\equiv r(\xi,1)$ (the second term in (57) involving the term $\frac{\partial\gamma_r^{(i)}}{\partial\xi}$) is neglected in [3], which is believed to be an error corrected in [4] (in Section 4.2.5 the full term is represented).

4. p-FEM implementation for axisymmetric domains

Contrary to the classical h-version of the FEM, in p-version the mesh is kept unchanged and the discretization error is reduced by increasing the polynomial degree of the shape functions. It has been proven mathematically and demonstrated by numerical examples that the p-version of the FEM converges faster than its h-version counterpart for linear elliptic problems [5]. In problems with smooth solutions, exponential convergence rates are realized i.e. by order of magnitudes faster compared to h-FEMs. Because the type of problems discussed herein have smooth solutions, and are being solved by linearization, it is anticipated that p-FEMs will carry over the high convergence rates shown in linear problems.

For completeness, we briefly outline in the next subsection two important features of p-FEMs. In p-FEMs the mesh is fixed, therefore the finite elements have to represent exactly the domain's boundary and each FE is mapped to the standard element by blending functions. In our p-version implementation the hierarchical basis functions in [5] are used, and the blending-function mapping of Gordon and Hall [18] is exploited. These two aspects of the p-FEMs are shortly summarized in the next subsection.

4.1. p-FEMs: Hierarchic shape functions and blending mappings

4.1.1. Hierarchic shape functions for quadrilateral elements

We define the *tensor product space* $\mathscr{S}_{\mathrm{ps}}^{p,p}(\Omega_{\mathrm{st}}^q)$ on the axi-symmetric (2-D) standard quadrilateral element shown in is Fig. 5. It consists of all the polynomials on $\Omega_{st}^q=[(-1,1)\times(-1,1)]$ spanned by the set of monomials $\xi^i\eta^j$ with $i=0,1,\ldots,p_\xi$ and $j=0,1,\ldots,p_\eta$. By construction, the two-dimensional shape functions can be classified into three groups:

(1) Nodal modes: The nodal modes

$$N_{1,1}^{N_i}(\xi,\eta)=\frac{1}{4}(1+\xi_i\xi)(1+\eta_i\eta),\quad i=1,\ldots,4 \tag{59}$$

are the standard bilinear shape functions, which are familiar from the isoparametric four-noded quadrilateral element. (ξ_i,η_i) denote the local coordinates of the ith node. Fig. 6 (left-hand side) depicts the mode for node 1.

(2) Edge modes: These modes are defined separately for each individual edge, they vanish at all other edges. The corresponding modes for edge 1 read:

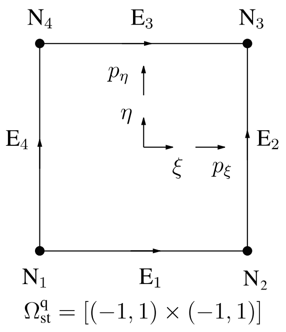

Fig. 5. Standard quadrilateral element: definition of nodes, edges and polynomial degree.

Node 1: Edge 1: $(i=2)$: Internal mode: $(i=j=2)$:

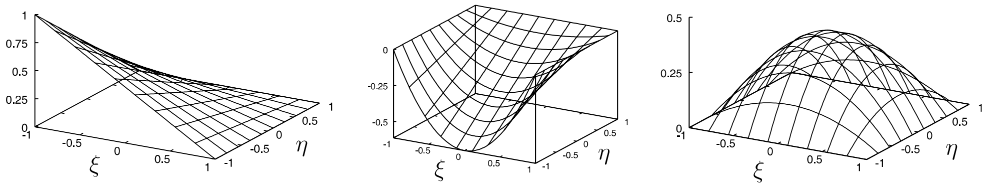

$N^{\mathrm{N}_1}_{1,1}(\xi,\eta)=\frac{1}{4}(1-\xi)(1-\eta)$ $N^{\mathrm{E}_1}_{2,1}(\xi,\eta)=\frac{1}{2}(1-\eta)\phi_2(\xi)$ $N^{\mathrm{int}}_{2,2}(\xi,\eta)=\phi_2(\xi)\phi_2(\eta)$

Fig. 6. Examples of hierarchical shape functions for quadrilateral elements.

$$N^{E_1}_{i,1}(\xi,\eta)=\frac{1}{2}(1-\eta)\phi_i(\xi) \tag{60}$$

with $\phi_i(\xi)$ given by (62). Fig. 6 (middle) plots the mode for edge 1 with $i=2$.

(3) Internal modes: The internal modes

$$N^{\mathrm{int}}_{i,j}(\xi,\eta)=\phi_i(\xi)\phi_j(\eta) \tag{61}$$

are purely local and vanish at the edges of the quadrilateral element. Fig. 6 (right-hand side) depicts the internal mode for $i=j=2$.

The indices i,j of the shape functions denote the polynomial degrees in the local directions ξ, η. The two-dimensional hierarchic shape functions are based on tensor products of

$$\begin{aligned}\phi_j(\xi)&=\sqrt{\frac{2j-1}{2}}\int_{-1}^{\xi}P_{j-1}(t)\,\mathrm{d}t\\&=\frac{1}{\sqrt{4j-2}}(P_j(\xi)-P_{j-2}(\xi)),\quad j=2,3,\ldots\end{aligned} \tag{62}$$

where $P_j(\xi)$ are the well-known Legendre polynomials

$$P_k(\xi)=\frac{1}{2^k k!}\frac{\mathrm{d}^k}{\mathrm{d}\xi^k}(\xi^2-1)^k,\quad k=0,1,\ldots \tag{63}$$

4.1.2. Two-dimensional blending mapping

An important difference between h- and p-FEMs lies in *the mapping requirements*. As coarse meshes are used in p-FEMs, it is necessary to construct elements with a precisely defined boundary. The *blending function method* [18] is applied when mapping *p*-finite elements with curved boundaries to the standard element. Consider for example a quadrilateral element with all edges being curved boundaries (see Fig. 7), described by parametric functions E_i, $i=1,2,3,4$:

$$E_{iR}(\xi),E_{iZ}(\xi),\quad \text{for } i=1,3,\quad E_{iR}(\eta),E_{iZ}(\eta),\quad \text{for } i=2,4. \tag{64}$$

The nodal coordinates of the element in the reference configuration are defined herein by $\boldsymbol{X}_i=(R_i,Z_i)^{\mathrm{T}}$, $i=1,2,3,4$. Mapping of the standard element to the physical element in the initial configuration by blending-functions is expressed in condensed form by $\boldsymbol{X}=\boldsymbol{\Gamma}(\xi,\eta)$, or explicitly by the two functions

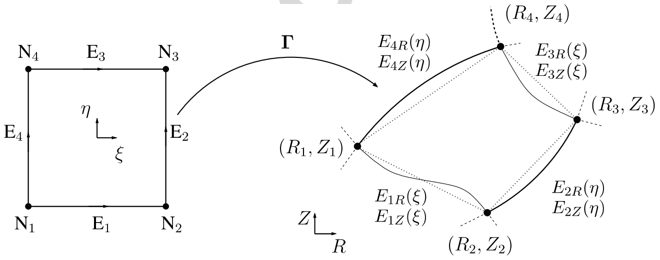

Fig. 7. Blending function method for quadrilateral elements.

$$\begin{aligned}R=\Gamma_R(\xi,\eta)&=\frac{1}{2}(1-\eta)E_{1R}(\xi)+\frac{1}{2}(1+\xi)E_{2R}(\eta)\\&\quad+\frac{1}{2}(1+\eta)E_{3R}(\xi)+\frac{1}{2}(1-\xi)E_{4R}(\eta)-\sum_{i=1}^{4}N^{N_i}_{1,1}(\xi,\eta)R_i\end{aligned} \tag{65}$$

$$\begin{aligned}Z=\Gamma_Z(\xi,\eta)&=\frac{1}{2}(1-\eta)E_{1Z}(\xi)\\&\quad+\frac{1}{2}(1+\xi)E_{2Z}(\eta)+\frac{1}{2}(1+\eta)E_{3Z}(\xi)\\&\quad+\frac{1}{2}(1-\xi)E_{4R}(\eta)-\sum_{i=1}^{4}N^{N_i}_{1,1}(\xi,\eta)Z_i\end{aligned} \tag{66}$$

The basic idea is to accurately represent the curved edge E. The blending function method allows for a large variety of element shapes with parametric functions (64) describing the geometry of the edges. In the reported example of the sphere (circle cross section in the axi-symmetric analysis) transcendental functions are used to exactly render the circular boundary E.

4.2. Implementing follower loads formulation into p-FEM framework

Consider the initial configuration, i.e. $\boldsymbol{\gamma}^{(0)}=\boldsymbol{\Gamma}(\boldsymbol{\xi})$, $\boldsymbol{\varphi}^{(0)}=0$. To solve the non-linear problem $G(\boldsymbol{\varphi},\boldsymbol{\psi},\alpha)=0$ for the prescribed load level α, we apply the Newton–Raphson iterative scheme and solve in each iteration i the linearized weak form

$$G(\boldsymbol{\varphi}^{(i)},\boldsymbol{\psi},\alpha)+DG(\boldsymbol{\varphi}^{(i)},\boldsymbol{\psi},\alpha)[\boldsymbol{\mu}^{(i)}]=0 \tag{67}$$

for the displacement update $\boldsymbol{\mu}^{(i)}$. In the next iteration the updated configuration $\boldsymbol{\varphi}^{(i+1)}=\boldsymbol{\varphi}^{(i)}+\ \boldsymbol{\mu}^{(i)}$ is used instead

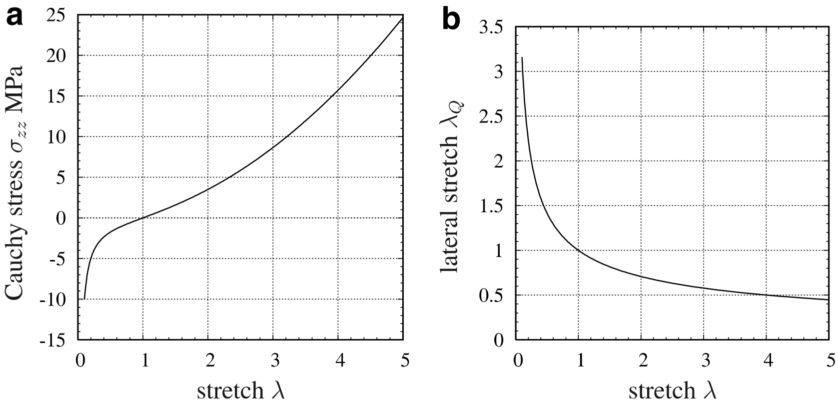

Fig. 8. Uniaxial behavior of the Neo-Hookean type model: (a) stress-stretch behavior and (b) stretch-lateral stretch behavior.

of $\boldsymbol{\varphi}^{(i)}$ in Eq. (67). The deformed configuration is obtained by

$$\boldsymbol{\gamma}^{(i+1)} = \boldsymbol{\gamma}^{(i)} + \boldsymbol{\mu}^{(i)} = \left[\boldsymbol{\Gamma}(\xi,\eta) + \sum_{j=0}^{i-1}\boldsymbol{\mu}^{(j)}\right] + \boldsymbol{\mu}^{(i)}. \tag{68}$$

The displacement vector $\boldsymbol{\mu}^{(i)}(\xi,\eta)$ is represented by the standard shape functions:

$$\boldsymbol{\mu}^{(i)}(\xi,\eta) = \begin{pmatrix}\mu_r^{(i)}\\ \mu_z^{(i)}\end{pmatrix} \overset{\text{def}}{=} \mathbf{N}\boldsymbol{m}^{(i)} \tag{69}$$

where $\mathbf{N}$ denotes the matrix of shape functions (one column for each generalized degree of freedom associated with a shape function) and $\boldsymbol{m}^{(i)}$ is the vector of the generalized d.o.f. at iteration i. The convergence of the iterative scheme can be established using a stopping criterion of the form:

$$\frac{\|\boldsymbol{\gamma}^{(i+1)} - \boldsymbol{\gamma}^{(i)}\|}{\|\boldsymbol{\gamma}^{(i+1)}\|} < \tau$$

or by monitoring the residual $G(\boldsymbol{\varphi}^{(i+1)},\boldsymbol{\psi},\alpha) < \tau$ where τ is a given small number. For other possible criteria see [19]. After convergence the next load level α can be set and the iterations start again until the total pressure is activated.

4.3. The load vector

The computation of the follower load vector at iteration i in (56) requires the following terms presented herein. The first term is

$$\begin{pmatrix}-\dfrac{\partial\gamma_z}{\partial\xi}\\[2mm] \dfrac{\partial\gamma_r}{\partial\xi}\end{pmatrix} = \begin{bmatrix}0 & -1\\ 1 & 0\end{bmatrix}\begin{pmatrix}\dfrac{\partial\gamma_r}{\partial\xi}\\[2mm] \dfrac{\partial\gamma_z}{\partial\xi}\end{pmatrix} \overset{\text{def}}{=} \mathbf{A}\frac{\partial\boldsymbol{\gamma}}{\partial\xi}. \tag{70}$$

Substituting (68) and (69) in (70), one obtains

$$\begin{pmatrix}-\dfrac{\partial\gamma_z^{(i)}}{\partial\xi}\\[2mm] \dfrac{\partial\gamma_r^{(i)}}{\partial\xi}\end{pmatrix} = \mathbf{A}\left[\frac{\partial\boldsymbol{\Gamma}(\xi,\eta)}{\partial\xi} + \sum_{j=0}^{i-1}\frac{\partial\boldsymbol{\mu}^{(j)}}{\partial\xi}\right] = \mathbf{A}\left[\frac{\partial\boldsymbol{\Gamma}(\xi,\eta)}{\partial\xi} + \sum_{j=0}^{i-1}\frac{\partial\mathbf{N}}{\partial\xi}\boldsymbol{m}^{(j)}\right]. \tag{71}$$

The second term $\gamma_r^{(i)}(\xi,\eta)$ in (56) can be represented by

$$\gamma_r^{(i)}(\xi,\eta) = (1\,0)\boldsymbol{\gamma}^{(i)} = (1\,0)\left[\boldsymbol{\Gamma}(\xi,\eta) + \sum_{j=0}^{i-1}\mathbf{N}\boldsymbol{m}^{(j)}\right]. \tag{72}$$

Finally, representing the test function $\boldsymbol{\psi}^{\mathrm{T}} = \boldsymbol{d}^{\mathrm{T}}\mathbf{N}^{\mathrm{T}}$ and substituting (70) and (72) in (56) we obtain the follower load vector at the ith iteration and load level α:

$$\begin{aligned}&\overline{G}(\boldsymbol{\varphi}^{(i)},\boldsymbol{\psi},\alpha)\\ &= \boldsymbol{d}^{\mathrm{T}}\int_{-1}^{1} -2\pi P(\alpha)\mathbf{N}^{\mathrm{T}}\mathbf{A}\left[\frac{\partial\boldsymbol{\Gamma}(\xi,1)}{\partial\xi} + \frac{\partial\mathbf{N}(\xi,1)}{\partial\xi}\sum_{j=0}^{i-1}\boldsymbol{m}^{(j)}\right](10)[\boldsymbol{\Gamma}(\xi,1)\\ &\quad + \mathbf{N}\sum_{j=0}^{i-1}\boldsymbol{m}^{(j)}]\mathrm{d}\xi.\end{aligned} \tag{73}$$

4.4. The tangent stiffness matrix

The tangent stiffness matrix is obtained from (58). The terms in the integrand of (58) are rearranged to the following form:

$$\begin{pmatrix}-\dfrac{\partial\mu_z^{(i)}}{\partial\xi}\gamma_r^{(i)} - \dfrac{\partial\gamma_z^{(i)}}{\partial\xi}\mu_r^{(i)}\\[2mm] \dfrac{\partial\mu_r^{(i)}}{\partial\xi}\gamma_r^{(i)} + \dfrac{\partial\gamma_r^{(i)}}{\partial\xi}\mu_r^{(i)}\end{pmatrix} = \gamma_r^{(i)}\mathbf{A}\frac{\partial\boldsymbol{\mu}^{(i)}}{\partial\xi} + \mathbf{A}\frac{\partial\boldsymbol{\gamma}^{(i)}}{\partial\xi}\mu_r^{(i)}. \tag{74}$$

Substituting the spatial discretization (71) and (72) in (74):

$$\begin{aligned}&\begin{pmatrix}-\dfrac{\partial\mu_z^{(i)}}{\partial\xi}\gamma_r^{(i)} - \dfrac{\partial\gamma_z^{(i)}}{\partial\xi}\mu_r^{(i)}\\[2mm] \dfrac{\partial\mu_r^{(i)}}{\partial\xi}\gamma_r^{(i)} + \dfrac{\partial\gamma_r^{(i)}}{\partial\xi}\mu_r^{(i)}\end{pmatrix}\\ &= \left\{(1\,0)\left[\boldsymbol{\Gamma}(\xi,\eta) + \mathbf{N}\sum_{j=0}^{i-1}\boldsymbol{m}^{(j)}\right]\mathbf{A}\frac{\partial\mathbf{N}}{\partial\xi}\right.\\ &\quad\left. + \mathbf{A}\left[\frac{\partial\boldsymbol{\Gamma}(\xi,\eta)}{\partial\xi} + \frac{\partial\mathbf{N}}{\partial\xi}\sum_{j=0}^{i-1}\boldsymbol{m}^{(j)}\right](1\,0)\mathbf{N}\right\}\boldsymbol{m}^{(i)}.\end{aligned} \tag{75}$$

The last step is to substitute (75) into (58) to obtain the tangent stiffness matrix for the ith iteration:

$$\begin{aligned} &D\overline{G}(\boldsymbol{\varphi}^{(i)},\boldsymbol{\psi},\alpha)[\boldsymbol{\mu}] \\ &\quad = \boldsymbol{d}^{\mathrm{T}}\int_{-1}^{1} -2\pi P(\alpha)\Bigg\{(1\,0)\Bigg[\boldsymbol{\Gamma}(\xi,1)+\mathbf{N}(\xi,1)\sum_{j=0}^{i-1}\boldsymbol{m}^{(j)}\Bigg] \\ &\qquad \times \mathbf{N}^{\mathrm{T}}(\xi,1)\mathbf{A}\frac{\partial \mathbf{N}(\xi,1)}{\partial\xi} \\ &\qquad + \mathbf{N}^{\mathrm{T}}(\xi,1)\mathbf{A}\Bigg[\frac{\partial\boldsymbol{\Gamma}(\xi,1)}{\partial\xi}+\frac{\partial\mathbf{N}(\xi,1)}{\partial\xi}\sum_{j=0}^{i-1}\boldsymbol{m}^{(j)}\Bigg] \\ &\qquad \times (1\,0)\mathbf{N}(\xi,1)\Bigg\}\boldsymbol{m}^{(i)}\,\mathrm{d}\xi. \end{aligned} \tag{76}$$

The mapping $\boldsymbol{\Gamma}$ in (73) and (76) is the blending function mapping.

4.5. The Newton–Raphson algorithm

For the numerical solution of the nonlinear weak form a Newton–Raphson algorithm is applied as described by [19]. Here a multilevel-approach is followed: given the deformation gradient the nonlinear hyperelastic constitutive relations at each integration point are solved by a local Newton algorithm yielding the stress state and consistent material tangent. Both are needed on global level to form the tangential stiffness matrix and residual vector. This nonlinear system is then solved by a Newton–Raphson algorithm on the global level where the tangential stiffness matrix and residual vector are recomputed in each iteration using the local stress algorithm.

5. Numerical tests comparing various solutions

In this section five verification examples for pressure-dependent loads on axisymmetric problems are provided, addressing the uniaxial tensile test, the thick-walled tube and sphere for a constant stress field, a thick-walled sphere under internal pressure as well as a plate under external pressure loads in out-of-plane direction. Except the last example, all problems are compared between analytical/semi-analytical or different numerical method and an h-version as well as a p-version finite element solution in order to show the ideas of verification as well as the performance of p-FEM applied to curved boundaries. In all applications the material parameters of the Neo-Hookean type model (6) are chosen to be $K = 2000$ MPa and $c_{10} = 0.5$ MPa.

5.1. Uniaxial tensile test

The simplest verification example problem for the axisymmetric setting is given by the uniaxial tensile problem of Section 2.1, see Fig. 1. There, the deformation-dependent load is pointed to the z-direction. Either this example can be chosen for code verification in displacement control or for pressure-prescribed problems as emphasized by the objective of the article. A single element with $p = 1$ (i.e. using an h-element) is sufficient to obtain the semi-analytical solution of Eqs. (12) and (13), see Fig. 8.

We have computed the FE solution using one element with both the h-FE code Abaqus/Implicit and the p-FE code *AdhoC* [20], verifying that the numerical results are identical to the analytical solution.

5.2. Thick-walled tube with a constant stress field

As a second verification example we consider the thick-walled tube under internal and external tractions, shown in Fig. 2(a), where the pressure load is applied in r-direction. According to (32) and (33), the applied tractions result in a constant stress field (32), i.e. a linear displacement behavior in r-direction. Therefore, again a single element of order $p = 1$ can be used to obtain the exact solution because of the homogeneous deformation. Accordingly, we checked the correct implementation by comparing the FE results to the exact solution, i.e. this example is only attributed to the correct implementation of the follower load. Thus, a comparison to the exact solution in form of a diagram can be omitted for brevity.

5.3. Thick-walled sphere with a constant stress field

In the following example, a thick-walled sphere under identical internal and external tractions is investigated. The analytical result defines a linear displacement field in radial direction and a constant hydrostatic stress field within the wall. This example addresses the influence of the boundary's curvature as well as the applied mesh on the accuracy of the displacement and stress field. Here, it has to be emphasized that the radial stresses differ from spherical to cylindrical coordinates so that the coordinate line $\varphi = 0$ has to be evaluated. In this example, a sphere with an inner radius $R_i = 10$ mm and an outer radius of $R_o = 30$ mm is chosen. From (34) we obtain for $A = 2$ a displacement field $u_r(R) = (A - 1)R$, corresponding to a radial stress of $\sigma_{rr} = -P = 14000$ MPa (the applied pressure is purely fictive and is only justified in view of a benchmark problem). Obviously, one p-element in combination with the blending function, which describes the exact geometry, has to provide the exact solution as the p level is increased. Consider the single element mesh presented in Fig. 9(a) and the schematic representation of the boundary conditions, with $u_\varphi(\varphi = \pi/2) = 0$. We performed a p-FE analysis with $p = 1$–8 with 10×10 Gauss points. Because of the $1/r$ term in the strains, the results at the axis of symmetry ($\varphi = 0$) are slightly different compared to $\varphi = \pi/2$. In Fig. 9(b) the convergence of the average displacements u_r in the thickness direction as a function of the number of degrees of freedom is provided. The averaged relative error over 101 points in the R direction of u_r is defined as

$$\text{Avg. error} \doteq \frac{1}{101}\sum_{j=1}^{101}\text{abs}\left(\frac{u_r^{EX}(R_j) - u_r^{FE}(R_j)}{u_r^{EX}(R_j)}\right) \tag{77}$$

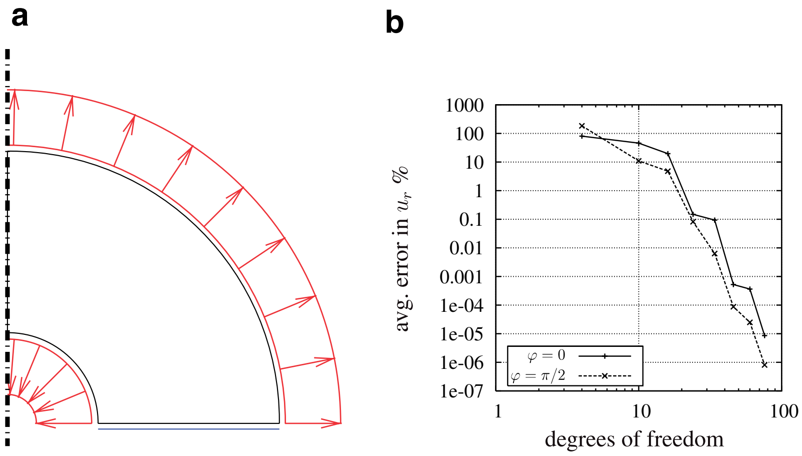

Fig. 9. Thick-walled sphere with a constant stress field $-P = 14{,}000$ MPa: (a) the single p-finite element and (b) convergence of averaged u_r at $\varphi = 0,\pi/2$.

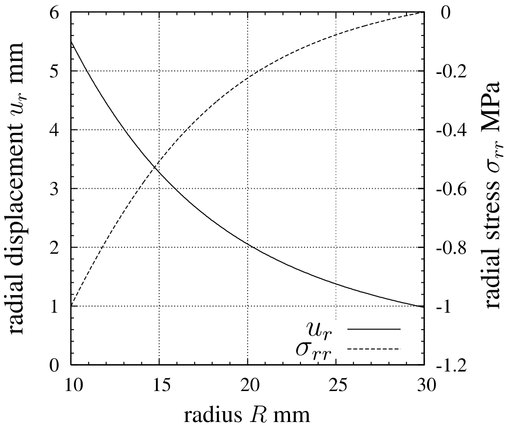

Fig. 10. "Exact" solution of thick-walled sphere under internal pressure $P = 1$ MPa.

One may notice the exponential convergence rate and the excellent results obtained with a very small number of degrees of freedom. Here, we attain a relative average error of less than 10^{-5} % for $p = 8$. This example problem demonstrates the efficiency of high-order methods for follower load applications when curved boundaries are considered.

5.4. Thick-walled sphere under internal pressure

A thick-walled sphere under internal pressure leads to an inhomogeneous deformation. The main goal of this example serves for the study of p- vs. h-finite elements. To this end, we define $R_i = 10$ mm, $R_o = 30$ mm and $-t_r^i = P = 1$ MPa. Use is made of the shooting method described in Section 2.2.2. There, an accuracy of 10^{-8} is obtained for the displacements. Defining the relative error in percentage (in u_r for example) at any R:

$$\varepsilon(u_r) \doteq \text{abs}\left(\frac{u_r^{EX} - u_r^{FE}}{u_r^{EX}}\right) \times 100 \tag{78}$$

we investigate p-FE vs. the h-FE results. For the p-FE analysis use is made of a single finite element as shown in Fig. 9(a), and the polynomial order is increased from 1 to 8. For the h-FE analysis three different h-meshes having 20×20, 40×40 and 80×80 linear elements are considered as shown in Fig. 11. The non-linear analyses are performed using 10 load-steps (each of 0.1 MPa). The relative error in the radial displacements along the sphere thickness between h-FE results and the exact solution is shown in Fig. 12(a). Although the geometry and boundary conditions are symmetric, the h-FE solution exhibits small differ-

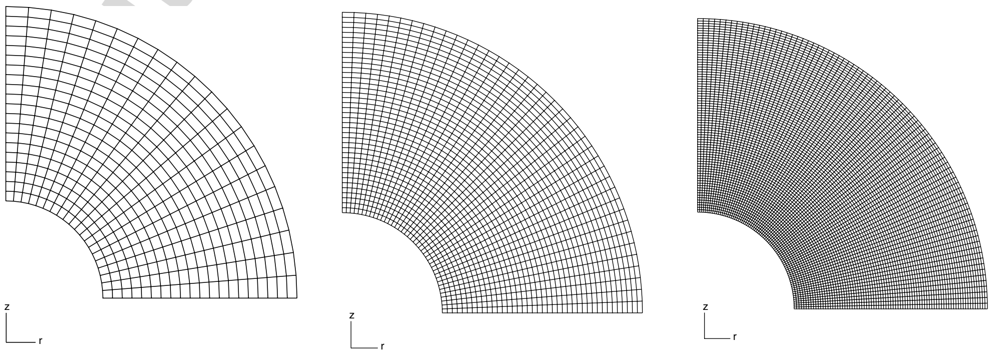

Fig. 11. 20×20, 40×40 and 80×80 h-meshes for the sphere problem under internal pressure.

ence when stresses are evaluated along the $z = 0$ axis or along the $r = 0$ axis. To demonstrate the phenomenon, we present in Fig. 12(b) the relative error in the Cauchy stress σ_{rr} compared to the exact solution at the two different axes. The same problem is solved on a 2-element mesh (shown in Fig. 13(a)) using p-FEMs. Increasing the

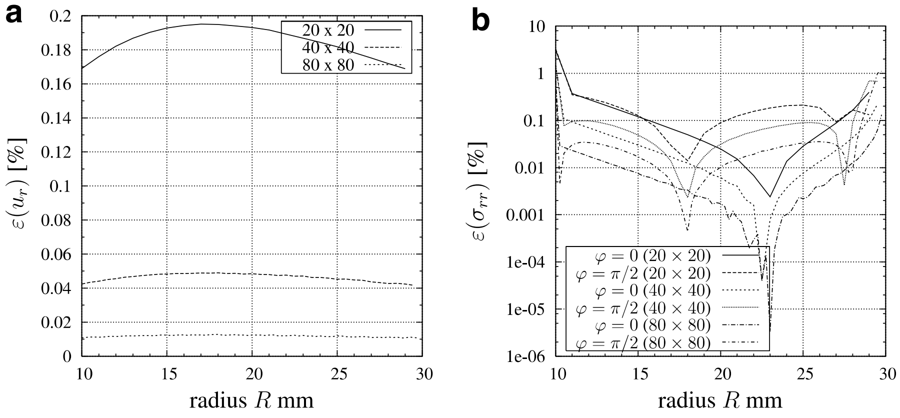

Fig. 12. Relative error behavior for different h-meshes: (a) h-FE results – relative error in u_r in percentage and (b) h-FE results – relative error in σ_{rr} in percentage.

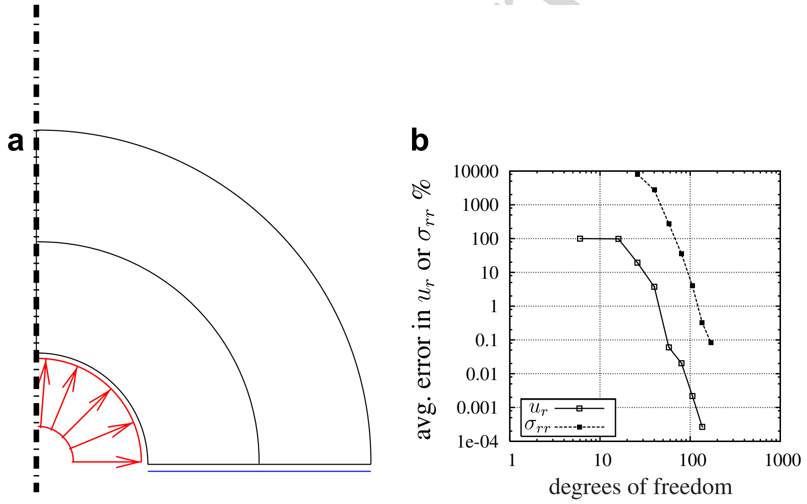

Fig. 13. p-FEA of thick-walled sphere under internal pressure, $P = 1$ MPa: (a) the p-FEM mesh consisting of two elements and (b) convergence of averaged u_r at $\varphi = \pi/2$ $p = 1$ to 8.

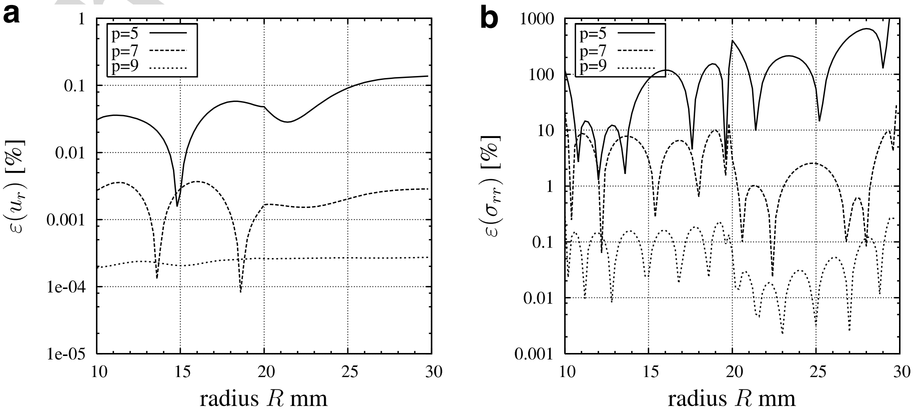

Fig. 14. Relative error across thickness for different p-levels using two elements in thickness direction: (a) p-FE results – relative error in u_r in percentage and (b) p-FE results – relative error in σ_{rr}.

Table 1
DOF and average relative errors (%) for h-FE and p-FE solutions

Abaqus		p-FEM mesh with two elements	
DOF (# el.)	Avg. error (u_r) %	DOF (p)	Avg. error (u_r) %
840 (20×20)	0.17	6 (1)	99.3941165
3280 (40×40)	0.04	16 (2)	98.0687522
12960 (80×80)	0.01	26 (3)	19.3433531
		40 (4)	3.7408152
		58 (5)	0.0600319
		80 (6)	0.0203799
		106 (7)	0.0021813
		136 (8)	0.0002665

polynomial order from 1 to 8, and using 15×15 integration points we present the convergence of the averaged u_r displacement across the thickness in Fig. 13(b). One may observe the exponential rate of convergence, obtaining a relative error of about 0.0002% with less than 200 DOFs. The pointwise relative errors (%) in displacements and stresses at $p = 5, 7, 9$ across the wall's thickness are presented in Figs. 14(a) and (b). In Fig. 13(b) the convergence of the average σ_{rr} stress along the thickness of the sphere for $p = 3$–9 is depicted. One may observe the exponential convergence rate in the stresses also. In Table 1 the number of degrees of freedom and the averaged error in displacement for both, the h- and p-extension are listed. It is important to mention that by using the displacement formulation for a nearly incompressible material ($K = 2000$) introduces large errors in the stress computation because the error in displacements are magnified by a factor of K (see (30)).

5.5. Pressure on a thin circular plate

Consider a circular plate clamped at its *outer* edge as shown in Fig. 15 on which a pressure of $P = 0.01$ MPa is acting on the upper surface, following the boundary's deformation. This example problem demonstrates both a change in the arc-length at which pressure is applied and the direction of the pressure, however no analytical solution is available for it. We compute the solution by 10 increments with Abaqus obtaining a deflection of 0.182571 at point A and a deflection of 0.178883 at point D, using 8-noded elements (100×10 elements), see Fig. 16. The same problem is computed by two different p-FE meshes, a 6-element and 8-element mesh – see Fig. 16. The deflections at the upper and lower center of the plate obtained by h-FE and p-FE methods are summarized in Table 2.

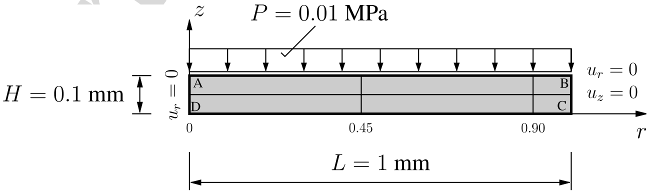

Fig. 15. Geometry and dimensions for the circular plate.

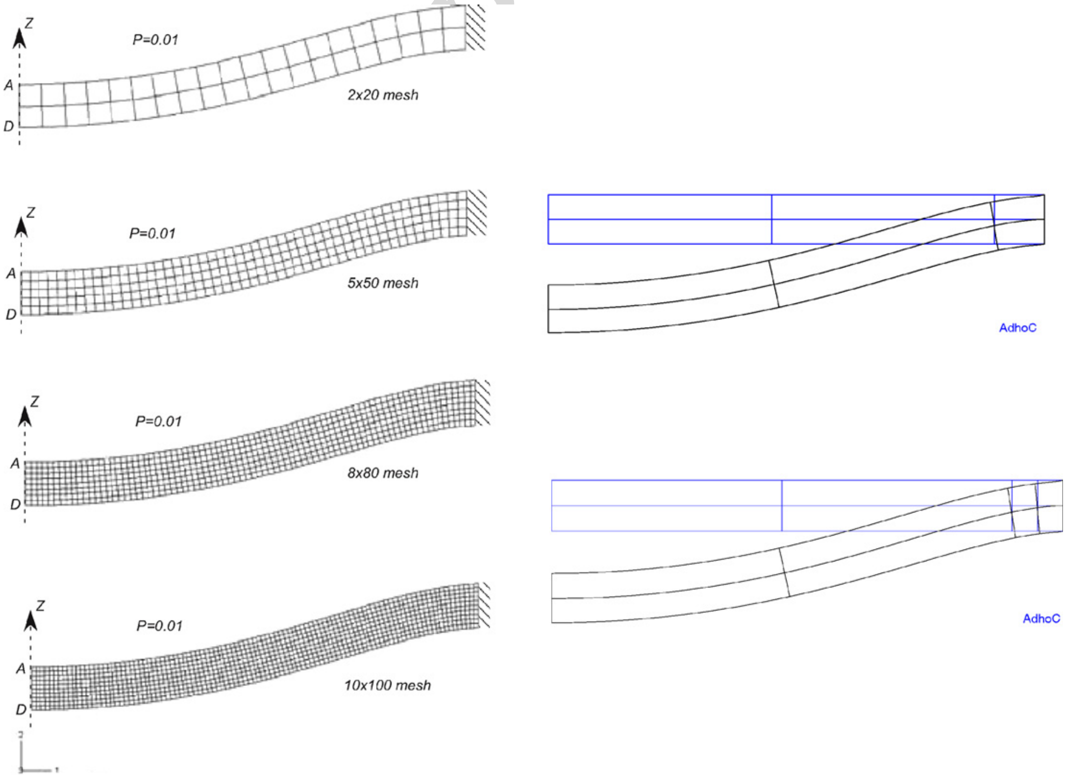

Fig. 16. Abaqus meshes (left), and AdhoC 6 and 8 elements meshes (right).

Table 2
Deflections at points *A* and *D* for the h-FE and two p-FE meshes

Abaqus			6 el mesh			8 el mesh		
DOF (# el. ; # iter.)	*A*	*D*	DOF (*p*)	*A*	*D*	DOF (*p*)	*A*	*D*
315 (2 × 20 ; 57)	−0.177739	−0.171180	15 (1)	−0.029559	−0.029552	21 (1)	−0.029818	−0.029809
1689 (5 × 50; 32)	−0.181917	−0.178249	43 (2)	−0.175045	−0.170344	59 (2)	−0.182626	−0.177907
4143 (8 × 80; 82)	−0.182409	−0.178729	71 (3)	−0.170592	−0.167631	97 (3)	−0.178841	−0.175423
6379 (10 × 100; 71)	−0.182571	−0.178839	111 (4)	−0.180264	−0.176697	151 (4)	−0.181775	−0.178166
			163 (5)	−0.181809	−0.178141	221 (5)	−0.182367	−0.178686
			227 (6)	−0.182250	−0.178575	307 (6)	−0.182550	−0.178866
			303 (7)	−0.182461	−0.178778	409 (7)	−0.182647	−0.178961

One may notice the convergence of both h- and p-FE methods, and the efficiency which is obtained when applying p-FEMs to finite deformation problems with follower loads.

6. Conclusions

The formulation, finite-element implementation and verification of pressure loads in the framework of a p-FE code have been addressed. We concentrate our attention on axisymmetric finite strain problems for which analytical solutions are obtained for a compressible Neo-Hooke material.

The purpose of this paper is three-fold: firstly, to derive analytical solutions for compressible axisymmetric problems with follower loads undergoing finite deformations against which the accuracy and efficiency of FE solutions can be assessed. Secondly, to formulate the weak form and finite element implementation in the framework of p-FE analysis utilizing the blending function technique which accurately represents the outer boundary on which the follower loads act. Finally, we compared the performance of p-FE on the basis of four problems with pressure loads having analytical (or semi-analytical) solution and also two more complicated problems for which an h-FE commercial code, Abaqus, was used. As to the efficiency, in terms of DOFs it is evident from the comparisons made that in order to achieve same accuracy p-FEMs require less than 10% compared to h-FE DOFs, and furthermore an exponential convergence rate is observed. In terms of CPU time, a direct comparison is difficult because the computer code AdhoC (p-FE solutions) runs under a Linux OS on a PC and Abaqus runs on a Win/XP OS on a different PC. Nevertheless, both machines are of comparable performance, and the CPU time required for the p-FE runs was shorter overall by about a factor of 10.

We demonstrated for finite strain problems with follower loads that p-FEMs produce results of high accuracy using very little degrees of freedom, and that the convergence rate in averaged displacements and stresses is exponential.

Acknowledgements

The authors gratefully acknowledge the support of this work by the German-Israeli Foundation for Scientific Research and Development under grant number I-700-26.10/2001.

Appendix A. The 2nd order ODE for a compressible hyperelastic axisymmetric problem

A general method for the derivation of the second order ODE for determining $f(R)$ in the case of a tube or a sphere is provided (general isotropic hyper-elasticity). First, the difference of the radial and circumferential stresses (19)–(21) is calculated according to the equilibrium conditions (22) using (24) and (25). These expressions depend on the functions α_i, $i = 0, 1, 2$, in (4) and their derivatives in a complicated manner. Therefore, the the chain rule is applied. For the general treatment, α_i in (4) are expressed as

$$\alpha_0 = 2w_3\mathbf{III}_{\boldsymbol{b}}^{1/2}, \quad \alpha_1 = 2(w_1 + w_2\mathbf{I}_{\boldsymbol{b}})\mathbf{III}_{\boldsymbol{b}}^{-1/2}, \\ \alpha_2 = -2w_2\mathbf{III}_{\boldsymbol{b}}^{-1/2}, \tag{A.1}$$

where we use the abbreviations

$$w_1 = \rho_R\frac{\partial\Psi}{\partial\mathbf{I}_{\boldsymbol{b}}}, \quad w_2 = \rho_R\frac{\partial\Psi}{\partial\mathbf{II}_{\boldsymbol{b}}}, \quad w_3 = \rho_R\frac{\partial\Psi}{\partial\mathbf{III}_{\boldsymbol{b}}}, \tag{A.2}$$

We use for convenience the notation

$$\alpha_i = \alpha_i(w_k(I_j(R,f(R),f'(R))),I_j(R,f(R),f'(R))), \begin{cases} i = 0,1,2 \\ k = 1,2,3 \\ j = 1,2,3 \end{cases} \tag{A.3}$$

where $I_1 = \mathbf{I}_{\boldsymbol{b}}$, $I_2 = \mathbf{II}_{\boldsymbol{b}}$, and $I_3 = \mathbf{III}_{\boldsymbol{b}}$. The invariants I_j, $j = 1, 2, 3$, see (17) or (18), are functions of R, $r = f(R)$, and $s = f'(r)$. In (25) the derivatives of α_i with respect to R are required, yielding

$$\frac{\mathrm{d}\alpha_i}{\mathrm{d}R} = \sum_{k=1}^{3}\sum_{j=1}^{3}\frac{\partial\alpha_i}{\partial w_k}\frac{\partial w_k}{\partial I_j}\left(\frac{\partial I_j}{\partial R} + \frac{\partial I_j}{\partial r}f'(R) + \frac{\partial I_j}{\partial s}f''(R)\right) \\ + \sum_{j=1}^{3}\frac{\partial\alpha_i}{\partial I_j}\left(\frac{\partial I_j}{\partial R} + \frac{\partial I_j}{\partial r}f'(R) + \frac{\partial I_j}{\partial s}f''(R)\right) \tag{A.4}$$

$$= a_{i1}(R,f(R),f'(R)) + a_{i2}(R,f(R),f'(R))f''(R) \tag{A.5}$$

with

$$a_{i1} = \sum_{j=1}^{3} \left(\left(\sum_{k=1}^{3} \frac{\partial \alpha_i}{\partial w_k} \frac{\partial w_k}{\partial I_j} \right) + \frac{\partial \alpha_i}{\partial I_j} \right) \left(\frac{\partial I_j}{\partial R} + \frac{\partial I_j}{\partial r} f'(R) \right) \tag{A.6}$$

$$a_{i2} = \sum_{j=1}^{3} \left(\left(\sum_{k=1}^{3} \frac{\partial \alpha_i}{\partial w_k} \frac{\partial w_k}{\partial I_j} \right) + \frac{\partial \alpha_i}{\partial I_j} \right) \frac{\partial I_j}{\partial s} \tag{A.7}$$

Obviously, all derivatives $\partial\alpha_i/\partial I_2 = 0$ vanish, which are only introduced for representational convenience. In addition, the derivatives

$$\frac{\partial \alpha_0}{\partial w_1} = 0 \quad \frac{\partial \alpha_0}{\partial w_2} = 0 \quad \frac{\partial \alpha_0}{\partial w_3} = 2I_3^{1/2} \tag{A.8}$$

$$\frac{\partial \alpha_1}{\partial w_1} = \frac{2}{I_3^{1/2}} \quad \frac{\partial \alpha_1}{\partial w_2} = \frac{2I_1}{I_3^{1/2}} \quad \frac{\partial \alpha_1}{\partial w_3} = 0 \tag{A.9}$$

$$\frac{\partial \alpha_2}{\partial w_1} = 0 \quad \frac{\partial \alpha_2}{\partial w_2} = -2I_3^{-1/2} \quad \frac{\partial \alpha_2}{\partial w_3} = 0 \tag{A.10}$$

and

$$\frac{\partial \alpha_0}{\partial I_1} = 0 \quad \frac{\partial \alpha_0}{\partial I_2} = 0 \quad \frac{\partial \alpha_0}{\partial I_3} = \frac{w_3}{I_3^{1/2}} \tag{A.11}$$

$$\frac{\partial \alpha_1}{\partial I_1} = \frac{2w_2}{I_3^{1/2}} \quad \frac{\partial \alpha_1}{\partial I_2} = 0 \quad \frac{\partial \alpha_1}{\partial I_3} = -\frac{w_1 + w_2 I_1}{I_3^{3/2}} \tag{A.12}$$

$$\frac{\partial \alpha_2}{\partial I_1} = 0 \quad \frac{\partial \alpha_2}{\partial I_2} = 0 \quad \frac{\partial \alpha_2}{\partial I_3} = \frac{w_2}{I_3^{3/2}} \tag{A.13}$$

are required. Accordingly,

$$\frac{\mathrm{d}\sigma_{rr}}{\mathrm{d}R} = \hat{c}(R, f(R), f'(R)) + \hat{d}(R, f(R), f'(R)) f''(R) \tag{A.14}$$

with

$$\hat{c}(R, f(R), f'(R)) = a_{01} + a_{11} f'^2(R) + a_{21} f'^4(R), \tag{A.15}$$

$$\begin{aligned} \hat{d}(R, f(R), f'(R)) &= a_{02} + a_{12} f'^2(R) + a_{22} f'^4(R) \\ &\quad + 2f'(R)(\alpha_1 + 2\alpha_2 f'^2(R)) \end{aligned} \tag{A.16}$$

is calculable. To evaluate (A.6) and (A.7) one needs the derivatives of the invariants in (17) or (18). Denoting $r = f(R)$ and $s = f'(R)$ one has for the tube

$$\frac{\partial I_1}{\partial R} = -\frac{2}{R}\left(\frac{f}{R}\right)^2 \frac{\partial I_1}{\partial r} = \frac{2}{R}\left(\frac{f}{R}\right) \frac{\partial I_1}{\partial s} = 2f' \tag{A.17}$$

$$\begin{aligned} \frac{\partial I_2}{\partial R} &= -\frac{2}{R}\left(\frac{f}{R}\right)^2 (1 + f'^2) \frac{\partial I_2}{\partial r} \\ &= \frac{2}{R}\left(\frac{f}{R}\right)(1 + f'^2) \frac{\partial I_2}{\partial s} = 2f'(R)\left(1 + \left(\frac{f}{R}\right)^2\right) \end{aligned} \tag{A.18}$$

$$\frac{\partial I_3}{\partial R} = -\frac{2}{R}\left(\frac{f}{R}\right)^2 f'^2 \frac{\partial I_3}{\partial r} = \frac{2}{R}\left(\frac{f}{R}\right) f'^2 \frac{\partial I_3}{\partial s} = 2\left(\frac{f}{R}\right)^2 f'. \tag{A.19}$$

In the case of the sphere these expression read:

$$\frac{\partial I_1}{\partial R} = -\frac{4}{R}\left(\frac{f}{R}\right)^2 \quad \frac{\partial I_1}{\partial r} = \frac{4}{R}\left(\frac{f}{R}\right) \quad \frac{\partial I_1}{\partial s} = 2f' \tag{A.20}$$

$$\begin{aligned} \frac{\partial I_2}{\partial R} &= -\frac{4}{R}\left(\left(\frac{f'f}{R}\right)^2 + \left(\frac{f}{R}\right)^4\right) \\ \frac{\partial I_2}{\partial r} &= \frac{4}{R}\left(\left(\frac{f'^2 f}{R}\right) + \left(\frac{f}{R}\right)^3\right) \quad \frac{\partial I_2}{\partial s} = 4f'\left(\frac{f}{R}\right)^2 \end{aligned} \tag{A.21}$$

$$\begin{aligned} \frac{\partial I_3}{\partial R} &= -\frac{4}{R}\left(\frac{f}{R}\right)^4 f'^2 \quad \frac{\partial I_3}{\partial r} = \frac{4}{R}\left(\frac{f}{R}\right)^3 f'^2 \\ \frac{\partial I_3}{\partial s} &= 2\left(\frac{f}{R}\right)^4 f' \end{aligned} \tag{A.22}$$

Combining (A.14) with (24), yields the second order ODE

$$f''(R) = \frac{1}{\hat{d}}\left(\gamma(\sigma_{\vartheta\vartheta} - \sigma_{rr})\frac{f'}{f} - \hat{c}\right), \tag{A.23}$$

where $\hat{c}$ and $\hat{d}$ are defined in (A.15) and (A.16). Additionally either traction or displacements BCs have to be taken into account. If internal and/or external traction BCs are considered ($t_r^i = -\sigma_{rr}(R_i)$ and $t_r^o = \sigma_{rr}(R_o)$) then

$$\begin{aligned} -t_r^i &= \widehat{\alpha_0}(R_i, f(R_i), f'(R_i)) \\ &\quad + \widehat{\alpha_1}(R_i, f(R_i), f'(R_i)) f'^2(R_i) + \widehat{\alpha_2}(R_i, f(R_i), f'(R_i)) f'^4(R_i) \end{aligned} \tag{A.24}$$

$$\begin{aligned} t_r^o &= \widehat{\alpha_0}(R_o, f(R_o), f'(R_o)) \\ &\quad + \widehat{\alpha_1}(R_o, f(R_o), f'(R_o)) f'^2(R_o) + \widehat{\alpha_2}(R_o, f(R_o), f'(R_o)) f'^4(R_o). \end{aligned} \tag{A.25}$$

Otherwise if displacements BCs are prescribed $u(R_i)$ and/or $u(R_o)$,

$$f(R_i) = R_i + u(R_i) \quad \text{and/or} \quad f(R_o) = R_o + u(R_o) \tag{A.26}$$

R_i and R_o are the inner and the outer radii, respectively. In other words, the BCs are highly non-linear functions of the function f and f' in the case of traction boundary conditions.

References

[1] H. Hibbitt, Some follower forces and load stiffness, Int. J. Numer. Method Engrg. 14 (1979) 937–941.

[2] K. Schweizerhof, P. Wriggers, Consistent linearization for path following methods in nonlinear FE analysis, Comput. Methods Appl. Mech. Engrg. 59 (1986) 261–279.

[3] J. Simo, R. Taylor, P. Wriggers, A note on finite-element implementation of pressure boundary loading, Commun. Appl. Numer. Methods 7 (1991) 513–525.

[4] P. Wriggers, Nichtlineare Finite-Elemente-Methoden, Springer, 2001.

[5] B.A. Szabó, I. Babuška, Finite Element Analysis, John Wiley & Sons, New York, 1991.

[6] B. Szabó, A. Düster, E. Rank, The p-version of the finite element method, in: E. Stein, R. de Borst, T. Hughes (Eds.), Encyclopedia of Computational Mechanics, 1, John Wiley & Sons, 2004, pp. 119–139 (Chapter 5).

[7] A. Düster, S. Hartmann, E. Rank, p-fem applied to finite isotropic hyperelastic bodies, Comput. Methods Appl. Mech. Engrg. 192 (2003) 5147–5166.

[8] S. Hartmann, P. Neff, Polyconvexity of generalized polynomial-type hyperelastic strain energy functions for near-incompressibility, Int. J. Solids Struct 40 (11) (2003) 2767–2791.

[9] M.M. Caroll, On obtaining closed form solutions for compressible nonlinearly elastic materials, Z. Angew. Math. Phys. (ZAMP) S46 (1995) S126–S145.

[10] C.O. Horgan, On axisymmetric solutions for compressible nonlinearly elastic solids, Z. Angew. Math. Phys. (ZAMP) S46 (1995) S107–S125.

[11] C.O. Horgan, Equilibrium solutions for compressible nonlinearly elastic materials, in: Y. Fu, R. Ogden (Eds.), Nonlinear Elasticity: Theory and Applications, Cambridge University Press, New York, 1995, pp. 135–159.

[12] W. Ehlers, G. Eipper, The simple tension problem at large volumetric strains computed from finite hyperelastic material laws, Acta Mech. 130 (1998) 17–27.

[13] C. Truesdell, W. Noll, The Non-Linear Field Theories of Mechanics, Encyclopedia of Physics, III/3, Springer Verlag, Berlin, 1965.

[14] R. Ogden, Non-Linear Elastic Deformations, Ellis Horwood, Chichester, 1984.

[15] G. Engeln-Müllges, F. Reutter, Formelsammlung zur Numerischen Mathematik mit Standard-FORTRAN 77-Programmen, B.I. Wissenschaftsverlag, Mannheim, 1986.

[16] K. Schweizerhof, E. Ramm, Displacement dependent pressure loads in nonlinear finite element analyses, Comput. Struct. 18 (1984) 1099–1114.

[17] J. Bonet, R. Wood, Nonlinear Continuum Mechanics for Finite Element Analysis, Cambridge University Press, New York, 1997.

[18] W.J. Gordon, C.A. Hall, Transfinite element methods: blending functions interpolation over arbitrary curved element domains, Numer. Math. 21 (1973) 109–129.

[19] O. Zienkiewicz, R. Taylor, The Finite Element Method – Solid Mechanics, Fifth ed., 2, Butterworth-Heinemann, 2000.

[20] A. Düster, H. Bröker, H. Heidkamp, U. Heißerer, S. Kollmannsberger, R. Krause, A. Muthler, A. Niggl, V. Nübel, M. Rücker, D. Scholz, AdhoC^4 – User's Guide, Lehrstuhl für Bauinformatik, Technische Universit'ät München (2004).